Revisiting the 150 MHz Radio Luminosity Function of Star-Forming Galaxies with LOFAR Deep Fields through a Refined Statistical Framework

Wenjie Wang, 1,2,3 Zunli Yuan, 1,2,3 Hongwei Yu, 1,2,3,4 Yang Liu, 5 Yu Luo, 1,2,3 and Puxun Wu 1,2,3

¹Department of Physics, School of Physics and Electronics, Hunan Normal University, Changsha 410081, China
²Key Laboratory of Low Dimensional Quantum Structures and Quantum Control, Hunan Normal University, Changsha 410081, China
³Hunan Research Center of the Basic Discipline for Quantum Effects and Quantum Technologies, Hunan Normal University, Changsha 410081, China

⁴Institute of Interdisciplinary Studies, Hunan Normal University, Changsha, Hunan 410081, China
⁵Purple Mountain Observatory, Chinese Academy of Sciences, Nanjing 210023, China

ABSTRACT

We present a comprehensive analysis of the 150 MHz radio luminosity function (LF) of star-forming galaxies (SFGs) using deep observations from the LOFAR Two-metre Sky Survey in the ELAIS-N1, Boötes, and Lockman Hole fields. Our sample comprises $\sim 56,000$ SFGs over 0 < z < 5.7. We first analyze the deepest field (ELAIS-N1), then jointly model all three fields while accounting for their distinct flux limits and selection functions. Using adaptive kernel density estimation (KDE), we reconstruct the LF continuously across redshift and luminosity without binning or parametric assumptions. The KDE results reveal clear signatures of joint luminosity and density evolution (LADE). Motivated by this, we construct and fit three parametric models—pure luminosity evolution (PLE) and two LADE variants—using a full maximum-likelihood method that includes completeness corrections and constraints from the local radio LF and Euclidean-normalized source counts (SCs). Model selection using Akaike and Bayesian Information Criteria strongly favors LADE over PLE. For ELAIS-N1, the more flexible LADE model (Model C) provides the best fit, while for the combined fields, the simpler Model B balances fit quality and complexity more effectively. Both LADE models reproduce the observed LFs and SCs across luminosity and flux density ranges, whereas PLE underperforms. We also identify a mild excess at the bright end of the LF, likely due to residual AGN contamination. This study demonstrates that combining KDE with parametric modeling offers a robust framework for quantifying the evolving radio LF of SFGs, paving the way for future work with next-generation surveys like the SKA.

Keywords: Galaxy evolution(594); Star formation(1569); Luminosity function(942); Radio continuum emission(1340)

1. INTRODUCTION

Star formation is one of the most fundamental processes driving galaxy evolution across cosmic time. Understanding when and how galaxies assemble their stellar mass offers key insight into the mechanisms that shape their histories, from the epoch of reionization

Corresponding author: Zunli Yuan

yzl@hunnu.edu.cn

Corresponding author: Hongwei Yu

hwyu@hunnu.edu.cn

 $(z\gtrsim 6)$ through the peak of cosmic activity at $z\sim 2$ and into the low-redshift Universe.

The star formation rate (SFR) can be traced across the electromagnetic spectrum (e.g., Kennicutt Jr 1998). Ultraviolet (UV) observations directly measure the light from newly formed massive stars and thus provide a sensitive probe of star formation out to high redshifts ($z \sim 11$; e.g., McLure et al. 2013; Oesch et al. 2018; Bouwens et al. 2021). However, UV-based SFR estimates require substantial corrections for dust extinction (Smail et al. 1997; Riechers et al. 2013). The absorbed UV photons are re-emitted at far-infrared (FIR) and submillimeter wavelengths, providing a complementary view of obscured star formation (Kennicutt Jr 1998).

Unfortunately, FIR and submillimeter surveys often suffer from low angular resolution, complicating the identification of faint sources. In recent years, additional tracers of star formation have emerged, including optical emission lines and radio continuum surveys (Ouchi et al. 2010; Drake et al. 2013; Schober et al. 2015; Aird et al. 2017).

Continuum radio observations offer a dust-unbiased view of ongoing star formation activity. Short-lived massive stars end their lives as supernovae whose remnants accelerate cosmic-ray electrons, producing synchrotron radiation detectable at frequencies below 30 GHz (e.g., Sadler et al. 1989; Tabatabaei et al. 2017). This emission correlates strongly with the infrared luminosity from star-forming regions, giving rise to the well-established far-infrared-radio correlation (e.g., Condon et al. 1991; Bell 2003), which holds over a broad range of galaxy luminosities and redshifts. Radio emission thus provides a powerful, extinction-free tracer of the SFR in galaxies (Magnelli et al. 2015; Calistro Rivera et al. 2017; Delvecchio et al. 2017; Algera et al. 2020).

Across the full suite of multiwavelength surveys described above, a critical quantity that can be derived is the cosmic star formation rate density (SFRD), defined as the total SFR per unit comoving volume. Observations show that the SFRD rises from high redshift, peaks around $z \sim 2$, and declines by an order of magnitude toward the present day (Madau et al. 1996; Haarsma et al. 2000; Madau & Dickinson 2014; Novak et al. 2017; van der Vlugt et al. 2022; Cochrane et al. 2023; Wang et al. 2024). Nevertheless, the precise behavior of the SFRD beyond $z \sim 3$ remains uncertain. UV-based studies suggest a steep decline (Bouwens et al. 2015; McLeod et al. 2016; Ishigaki et al. 2018), whereas radio and submillimeter surveys sometimes indicate a more gradual decrease (Gruppioni et al. 2013, 2020; Rowan-Robinson et al. 2016; Novak et al. 2017; Enia et al. 2022). This tension points to the need for complementary, multiwavelength approaches to mitigate observational biases and better understand the underlying physics.

Traditional radio surveys at 1.4 GHz can already probe star formation over a wide range of redshift. However, since radio emission is redshifted to lower frequencies at high redshift, observations at 150 MHz provide a complementary view of star formation in the early Universe (Pritchard & Loeb 2010). Consequently, several recent efforts have shifted toward low-frequency radio surveys to assess the universal validity of radio-based SFR indicators (e.g., Gürkan et al. 2018; Ocran et al. 2020; Smith et al. 2021). Deep 150 MHz observations from the Low Frequency Array (LOFAR) Two-metre Sky Survey (LoTSS) now routinely reach μ Jy sensitivi-

ties, enabling statistically robust measurements of star-forming galaxies (SFGs) out to $z\gtrsim 5$ (e.g., Cochrane et al. 2023).

To quantify the cosmic star formation history in a physically meaningful way, one requires accurate measurements of the SFRD across redshift. A foundational ingredient for such measurements is the radio luminosity function (LF) of SFGs, which describes the number density of galaxies as a function of luminosity and redshift. By measuring the LF and integrating it over the full luminosity range, one can derive the SFRD at each epoch. Early studies often assumed pure luminosity evolution (PLE) (e.g., Smolčić et al. 2009; Novak et al. 2017; Ocran et al. 2020; Malefahlo et al. 2022), whereas more recent analyses have considered models combining both luminosity and density evolution (LADE) (van der Vlugt et al. 2022; Cochrane et al. 2023; Wang et al. 2024). Most of these works estimate the LF using the classical $1/V_{\text{max}}$ method (Schmidt 1968), which provides a convenient but binned representation of the underlying distribution.

In this work, we revisit the 150 MHz radio LF of SFGs using the same deep LOFAR observations from the ELAIS-N1, Boötes, and Lockman Hole fields as in Cochrane et al. (2023). While that study represents a major step forward in assembling large, well-characterized SFG samples at low radio frequencies, it relies on a two-step procedure: deriving LF points using the $1/V_{\rm max}$ method, and subsequently fitting those binned values with parametric models. This indirect approach, though widely used (e.g., Smolčić et al. 2009; Novak et al. 2017; Ocran et al. 2020; Malefahlo et al. 2022; van der Vlugt et al. 2022), introduces binning-related uncertainties and does not make full use of the statistical information encoded in the unbinned data (Fan et al. 2001).

To overcome these limitations, we adopt a statistically rigorous framework that combines non-parametric and parametric approaches. Specifically, we first apply adaptive kernel density estimation (KDE) (Yuan et al. 2020, 2022) to reconstruct the LF continuously across redshift and luminosity. Guided by the empirical trends revealed by the KDE, we then construct physically motivated LF models and constrain them using a full maximum-likelihood method that incorporates completeness corrections and additional constraints from the local radio LF and Euclidean-normalized source counts (SCs). This approach enables a more accurate and robust characterization of the evolving radio LF and maximizes the scientific return from existing deep surveys.

This paper is structured as follows. Section 2 describes the LOFAR data and multiwavelength ancillary

catalogues. Section 3 outlines our KDE framework and maximum-likelihood modeling approach. The resulting LFs and their evolution are presented in Section 4, while Section 5 discusses the implications of our findings and summarizes our conclusions. Throughout, we adopt a flat Λ CDM cosmology with $H_0=70~{\rm km\,s^{-1}\,Mpc^{-1}}$, $\Omega_{\Lambda}=0.7$, and $\Omega_m=0.3$, and assume a power-law radio spectrum $F_{\nu}\propto \nu^{-\alpha}$ with $\alpha=0.7$ where required.

2. SAMPLE

In this work, we use the same sample of SFGs presented in Cochrane et al. (2023), which was derived from deep 150 MHz observations of the ELAIS-N1, Boötes, and Lockman Hole fields, conducted as part of the LOFAR Two-metre Sky Survey (LoTSS) Deep Fields project. The data analysis and multi-band association procedure are fully described in Cochrane et al. (2023), and readers are referred to this work for further details. Here we summarize some key points about the sample.

The radio data were obtained using the LOFAR High-Band Antenna (HBA) array, with integration times of 164 hr, 80 hr, and 112 hr for ELAIS-N1, Boötes, and Lockman Hole, respectively, achieving rms sensitivities of $20 \,\mu \mathrm{Jy/beam}$, $32 \,\mu \mathrm{Jy/beam}$, and $22 \,\mu \mathrm{Jy/beam}$ at the pointing centers (Tasse et al. 2021; Sabater et al. 2021). The observations cover areas of approximately 25 deg² per field (within the 30% power point), with an angular resolution of 6". Source extraction was performed using PyBDSF (Mohan & Rafferty 2015), yielding initial catalogs of 84, 862, 36, 767, and 50, 112 radio sources for ELAIS-N1, Boötes, and Lockman Hole, respectively.

This sample is complemented by extensive multiwavelength data from UV to FIR, compiled and crossmatched by Kondapally et al. (2021). Photometric coverage includes UV data from GALEX (Martin et al. 2005), optical data from surveys such as Pan-STARRS (Chambers et al. 2016) and NDWFS (Weymann et al. 1999), near-IR data from UKIDSS-DXS (Lawrence et al. 2007) and NEWFIRM (Gonzalez 2010), and mid-to-far-IR data from *Spitzer* (Lonsdale et al. 2003; Ashby et al. 2009) and Herschel (Oliver et al. 2012). Photometric redshifts were derived using a hybrid approach combining template fitting and machine learning, as detailed in Duncan et al. (2021), with spectroscopic redshifts available for $\sim 8.6\%$ of sources. Cross-matching of radio sources to multiwavelength counterparts was limited to regions with optimal photometric coverage: $6.74 \, \mathrm{deg}^2$ in ELAIS-N1, 8.63 deg² in Boötes, and 10.28 deg² in Lockman Hole (Kondapally et al. 2021). Classification of SFGs and active galactic nuclei (AGN) was performed using multiple methods, including SED fitting with codes such as MAGPHYS, BAGPIPES, AGNfitter,

and CIGALE (Best et al. 2023), alongside radio-excess criteria based on the 150 MHz luminosity-to-SFR relation. SFGs were defined as sources lacking significant AGN signatures in optical/IR/X-ray and radio excess. For a detailed account of the observations, data processing, and sample selection, see Cochrane et al. (2023), Tasse et al. (2021), Sabater et al. (2021), Kondapally et al. (2021), and Best et al. (2023).

After cross-matching and filtering, the final sample comprises 55,991 SFGs with redshifts ranging from 0.001 < z < 5.7, including 21,725 in the ELAIS-N1 field, 12,895 in the Boötes field, and 21,371 in the Lockman Hole field. All the sources have (spectroscopic or photometric) redshifts and the rest-frame 150 MHz luminosities. The redshift distribution of the SFG sample as well as its scatter plot are shown in Figure 1. The red dashed curve indicates the 150 MHz flux limit line defined as

$$f_{\text{lim 150MHz}}(z) = \frac{4\pi D_L^2}{(1+z)^{1-\alpha}} F_{\text{lim 150MHz}},$$
 (1)

where D_L represents the luminosity distance at redshift z, and $\alpha=0.7$ is adopted for the K-correction. For illustration, we take the nominal central sensitivities of the LoTSS Deep Fields as $F_{\rm lim~150MHz}=100~\mu{\rm Jy}$ for ELAIS-N1, 160 $\mu{\rm Jy}$ for Boötes, and 110 $\mu{\rm Jy}$ for Lockman Hole (Cochrane et al. 2023). Since the noise increases away from the pointing centre, these values do not represent the true local 5σ threshold across the entire field. Instead, we use them as conservative reference limits to exclude sources lying below the corresponding flux—redshift curve, so that our analysis focuses on the most complete part of the survey.

3. METHODS

The LF, $\Phi(z, L)$, is defined as the number of sources per unit comoving volume V(z) per unit logarithmic luminosity interval $\log L$, i.e.,

$$\Phi(z, L) = \frac{d^2N}{dV \, d\log L}.\tag{2}$$

Methods for estimating the LF can be broadly classified into two categories: parametric and non-parametric approaches. Non-parametric methods, such as the classical $1/V_{\rm max}$ estimator (Schmidt 1968) and the more recent KDE method proposed by Yuan et al. (2020, 2022), are data-driven and make minimal assumptions about the underlying form of the LF. They are particularly useful for revealing unexpected structures in the data without being constrained by pre-imposed model forms.

Parametric methods, by contrast, assume a specific functional form for the LF and typically rely on

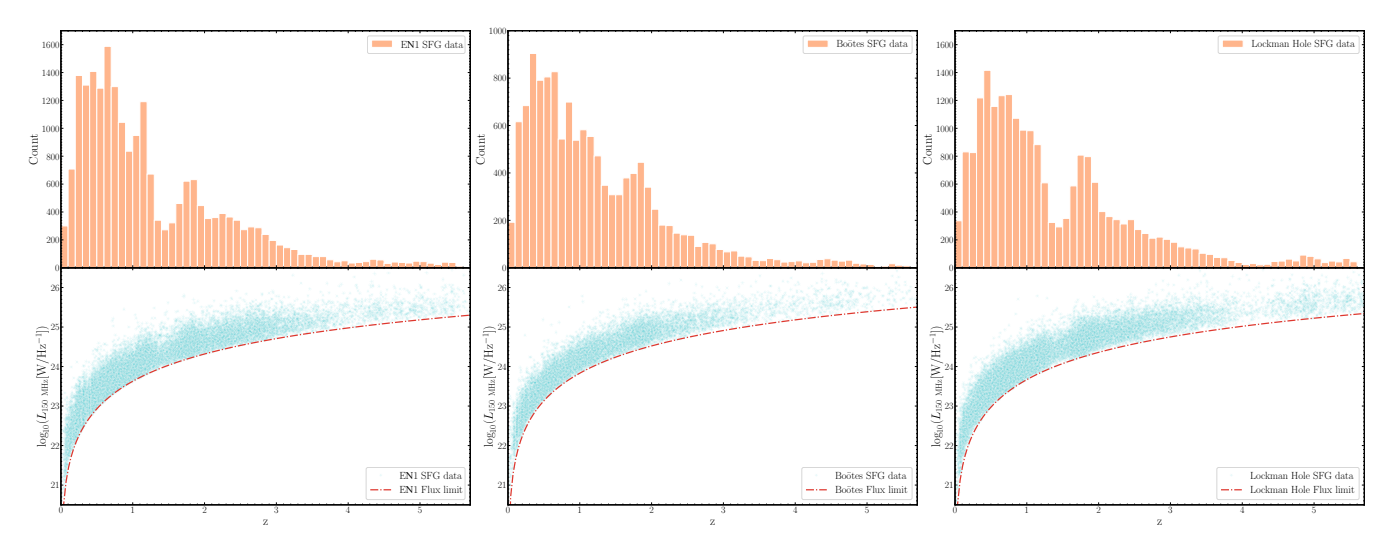


Figure 1. Redshift distribution (top) and scatter plot (bottom) of our SFG sample for three fields: ELAIS-N1 (left), Boötes (middle), and Lockman Hole (right). The red dashed lines indicate the flux limits of $F_{150\,\mathrm{MHz}} = 100\,\mu\mathrm{Jy}$ for ELAIS-N1, 160 $\mu\mathrm{Jy}$ for Boötes, and 110 $\mu\mathrm{Jy}$ for Lockman Hole. Note that a small number of sources fall below these flux limit lines and are excluded from our subsequent analysis.

maximum-likelihood estimation (MLE) to determine model parameters. When the assumed model closely resembles the true underlying distribution, this approach can yield highly accurate and efficient estimates. However, in practice, we seldom know the true form of the LF a priori, and inappropriate model choices may lead to biased results.

Therefore, it is often advantageous to combine both approaches. We can first use a non-parametric method (e.g., KDE) to obtain a smooth, empirical estimate of the LF shape, and then use this insight to guide the selection of a suitable parametric model. In the following, we briefly introduce the non-parametric KDE method and the parametric maximum-likelihood approach adopted in this work.

3.1. KDE-Based Luminosity Function Estimation

Mathematically, KDE is a statistically rigorous, non-parametric approach for reconstructing continuous density functions without assuming a specific parametric form, and has been extensively studied in the statistical literature (e.g. Wasserman 2006; Chen 2017; Davies & Baddeley 2018). Based on the principles of KDE, Yuan et al. (2020, 2022) proposed a flexible framework for estimating LFs, hereafter referred to as the KDE method. This method does not require any model assumptions, since it generates the LF relying only on the available data.

Given a two-dimensional dataset of redshift and luminosity points, (z_i, L_i) for i = 1, 2, ..., n, directly applying KDE can introduce boundary biases due to truncation. To mitigate this, a transformation-reflection method is

employed, mapping the data into an unbounded space:

$$x = \ln\left(\frac{z - Z_1}{Z_2 - z}\right), \quad y = L - f_{\lim}(z), \tag{3}$$

where $f_{\text{lim}}(z)$ denotes the luminosity truncation boundary at redshift z.

The KDE method is then applied to the transformed data in the (x, y) space. The density of (x, y), denoted as $\hat{f}(x, y)$, can be estimated by

$$\hat{f}(x,y) = \frac{1}{nh_1h_2} \sum_{j=1}^{n} \left(K\left(\frac{x-x_j}{h_1}, \frac{y-y_j}{h_2}\right) + K\left(\frac{x-x_j}{h_1}, \frac{y+y_j}{h_2}\right) \right)$$
(4)

To further improve the estimation accuracy, especially in cases where the data distribution is highly inhomogeneous, the density of (x,y) can also be estimated using adaptive bandwidths, leading to the so-called adaptive KDE, denoted as $\hat{f}_{\rm a}(x,y)$. In this approach, the smoothing parameters are allowed to vary across different data points depending on the local density, such that smaller bandwidths are used in dense regions and larger ones in sparse regions. Specifically, a pilot estimate $\tilde{f}(x,y)$ is first obtained using the fixed-bandwidth KDE. Then, the local bandwidths are modulated according to

$$\lambda_1(x_j, y_j) = h_{10}\tilde{f}(x_j, y_j)^{-\beta},$$
 (5)

$$\lambda_2(x_i, y_i) = h_{20}\tilde{f}(x_i, y_i)^{-\beta},$$
 (6)

where h_{10} and h_{20} are global scaling factors and β is a sensitivity parameter controlling the degree of adaptation ($0 \le \beta \le 1$). This scheme enables the estimator to

adaptively balance bias and variance across the domain, effectively mitigating both oversmoothing in dense areas and undersmoothing in sparse regions.

Once the adaptive bandwidths are determined, the density of (x, y) can be estimated by an adaptive KDE, denoted as $\hat{f}_a(x, y)$. Its mathematical form follows the same structure as Equation (4), with the fixed bandwidths h_1 and h_2 replaced by the location-dependent adaptive bandwidths $\lambda_1(x_j, y_j)$ and $\lambda_2(x_j, y_j)$ for each kernel term.

Transforming back to the original coordinates, the density of (z, L) can be written as

$$\hat{p}_{a}(z,L) = \hat{f}_{a}(x,y) \cdot \frac{Z_2 - Z_1}{(z - Z_1)(Z_2 - z)},$$
(7)

and the adaptive estimate of the LF becomes

$$\hat{\phi}_{a}(z,L) = \frac{n(Z_2 - Z_1)\hat{f}_{a}(x,y)}{(z - Z_1)(Z_2 - z)\Omega\frac{dV}{dz}},$$
(8)

where dV/dz is the differential comoving volume per unit solid angle, and Ω is the survey solid angle. The optimal values of h_{10} , h_{20} , and β are obtained by minimizing a likelihood cross-validation (LCV) objective function tailored to the transformation-reflection framework (for the full mathematical treatment, see Yuan et al. 2022).

3.2. Parametric Luminosity Function Modeling

While non-parametric methods such as KDE provide flexible, data-driven estimates of the LF, they do not directly yield a parametric form that can be used for extrapolation or theoretical interpretation. To this end, we also adopt a parametric approach based on MLE, which allows for the inference of model parameters within an assumed analytical form of the LF.

Given a model LF $\Phi(z, L \mid \boldsymbol{\theta})$ parameterized by $\boldsymbol{\theta}$, the optimal parameter values can be obtained by maximizing the likelihood function constructed from the observed data. Following the formalism of Marshall et al. (1983) and Fan et al. (2001), the negative log-likelihood for a single field is given by

$$S_{\text{single}} = -2 \sum_{i=1}^{n} \ln[\Phi(z_i, L_i) \, p(z_i, L_i)] + 2 \iint_{W} \Phi(z, L) \, p(z, L) \, \Omega[F(z)] \, \frac{dV}{dz} \, dz \, dL,$$
(9)

where p(z,L) is the selection probability of a SFG at redshift z and luminosity L, and W denotes the effective survey region in the (z,L) plane. The first term evaluates the likelihood at the observed data points, while the second term accounts for the expected number of

sources over the survey volume. $\Omega[F(z)]$ is the sky area over which a source with flux F can be detected at 5σ significance (Kondapally et al. 2021), and dV/dz is the differential comoving volume per unit solid angle (Hogg 1999).

For our SFG sample, the selection function p(z, L) is modeled as

$$p(z, L) = C_{\text{radio}}[F(z)] \times C_{\text{photometric}}(z),$$
 (10)

where $C_{\rm radio}[F(z)]$ describes the radio completeness of the LOFAR catalogue as a function of flux density, and $C_{\rm photometric}(z)$ is an empirical correction for photometric redshift errors such as aliasing (Cochrane et al. 2023). We adopt the tabulated values and procedures from Cochrane et al. (2023), and refer the reader to their Fig. 2 and Fig. 3 for details.

Equation (9) applies to a single field with well-defined completeness. In this work, we apply it specifically to the ELAIS-N1 field, which benefits from the deepest radio observations among the three. For a more comprehensive analysis, we also perform a joint fit combining all three sub-samples—ELAIS-N1, Boötes, and Lockman Hole. Given the differences in flux limits, survey areas, and selection functions, these fields cannot be merged at the catalogue level. Instead, their contributions are combined at the likelihood level, with each field treated using its respective completeness and sky coverage. The resulting total negative log-likelihood is

$$S_{\text{all}} = -2 \sum_{j} \sum_{i=1}^{n_j} \ln[\Phi_j(z_i, L_i) \, p_j(z_i, L_i)]$$

$$+2 \sum_{j} \iint_{W_j} \Phi_j(z, L) \, p_j(z, L) \, \Omega_j[F(z)] \, \frac{dV}{dz} \, dz \, dL,$$
(11)

where the index j runs over the three fields, n_j is the number of sources in field j, and all quantities— Φ_j , p_j , Ω_j , W_j —are field dependent. In our implementation, we consider both field-dependent LFs (Φ_j varying with j), and a simplified scenario where all three fields share a common LF, $\Phi_j \equiv \Phi$, to improve statistical constraints while accounting for field-specific incompleteness.

For the selection function p(z, L) in both Equations (9) and (11), we follow the interpolation-based approach developed in our previous work (Wang et al. 2024), which effectively captures the complex selection boundaries in the (z, L) plane.

While Equations (9) and (11) provide a statistical framework for fitting the (z, L) distribution of the sample, they are not the final objective functions adopted in this study. To further improve the parameter constraints and break degeneracies in redshift and luminosity, we incorporate two additional one-dimensional observational

constraints: (1) the local radio luminosity function (LRLF) of SFGs, and (2) the Euclidean-normalized radio source counts (SCs) in the ELAIS-N1 field. This choice is motivated by the limited depth of our radio data: even in the deepest ELAIS-N1 field, the sample does not reach the knee of the LF at $z \geq 0.5$, leaving the faint-side normalization and slope poorly constrained when relying on the catalog likelihood alone. In such an incompletely sampled regime, strong degeneracies arise between ϕ_{\star} , L_{\star} , and the redshift-evolution parameters. The independently measured LRLF at $z \simeq 0.1$ provides a robust local anchor for the low-luminosity end, while the Euclidean-normalized SCs add complementary information by constraining the luminosity- and redshiftintegrated abundance and are particularly sensitive to the space density of faint systems. Assuming Gaussian measurement uncertainties, including these data as additional χ^2 terms is equivalent to multiplying the corresponding likelihoods, thereby regularizing the fit with well-motivated external information and preventing unphysical extrapolation. Following Willott et al. (2001) and Yuan et al. (2017), we implement these constraints as additional χ^2 penalty terms in the likelihood function, each defined as

$$\chi^2 = \sum_{i=1}^n \left(\frac{f_{\text{data},i} - f_{\text{mod},i}}{\sigma_{\text{data},i}} \right)^2, \tag{12}$$

where $f_{\text{data},i}$ is the observed value in the *i*th bin, $f_{\text{mod},i}$ is the corresponding model prediction, and $\sigma_{\text{data},i}$ is the observational uncertainty. For the SCs, the term $f_{\text{mod},i}$ is obtained from Equation (14) by integrating the evolving LF over luminosity and redshift, while for the LRLF it is given by Equation (16), corresponding to the Saunders et al. (1990) form evaluated at z=0.10.

The final objective functions used for parameter estimation are given by:

$$S_{\text{single final}} = S_{\text{single}} + \chi_{\text{LRLF}}^2 + \chi_{\text{SC EN1}}^2,$$

$$S_{\text{all final}} = S_{\text{all}} + \chi_{\text{LRLF}}^2 + \chi_{\text{SC all}}^2,$$
(13)

where $\chi^2_{\rm LRLF}$ and $\chi^2_{\rm SC}$ denote the χ^2 contributions from the LRLF and SCs, respectively. These augmented likelihood functions serve as the final basis for model fitting in both the single-field and combined-field analyses.

To evaluate $\chi^2_{\rm LRLF}$, we use the binned measurements of the LRLF at 150 MHz from Cochrane et al. (2023), based on deep LOFAR observations at $z \lesssim 0.1$. The data points used in our modeling are shown in Figure 7.

To compute $\chi^2_{\rm SC~EN1}$ and $\chi^2_{\rm SC~all}$, we derive the 150 MHz Euclidean-normalized SCs using flux density distributions from the ELAIS-N1 field and the combined sample across all fields, respectively, both based

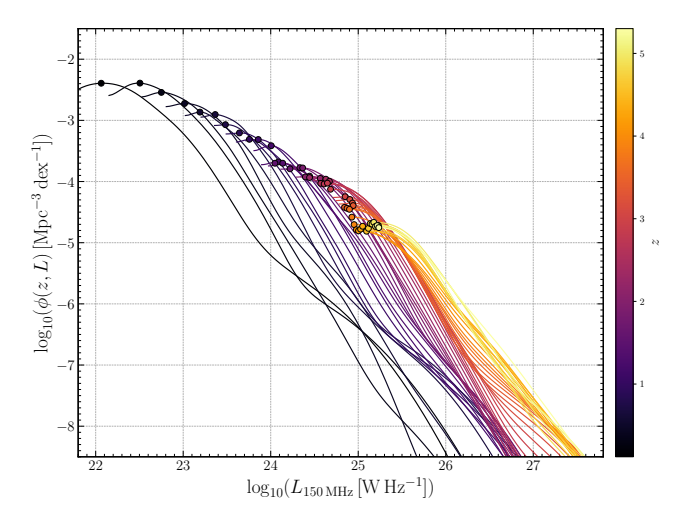


Figure 2. LFs estimated at a series of redshift grid points using the adaptive KDE method. The resulting curves are color-coded according to redshift. Solid circles indicate the flattest regions of the LF at each redshift.

on Cochrane et al. (2023). These binned measurements help constrain the global normalization and redshift evolution of the LF. The resulting SCs are shown in Figure 8.

Following Padovani (2016) and Yuan et al. (2017), the differential SCs $n(F_{\nu})$ are related to the evolving LF $\Phi(z, L)$ via

$$\begin{split} \frac{n(F_{\nu})}{4\pi} = & 4\pi \, \frac{c}{H_0} \times \\ & \int_{z_{\min}(F_{\nu})}^{z_{\max}(F_{\nu})} \frac{\Phi(z, L(F_{\nu}, z)) \, D_L^4(z)}{(1+z)^{3-\alpha} \sqrt{\Omega_{\mathrm{m}}(1+z)^3 + \Omega_{\Lambda}}} \frac{(14)}{dz}, \end{split}$$

where c is the speed of light, $D_L(z)$ is the luminosity distance, α is the spectral index, and z_{\min} and z_{\max} denote the redshift integration limits for a given flux density F_{ν} .

Using Equation (13), we determine the best-fit LF parameters by minimizing $S_{\text{single final}}$ and $S_{\text{all final}}$, respectively. The parameter space is explored using a Markov Chain Monte Carlo (MCMC) method with uniform (i.e., uninformative) priors, following the Bayesian framework of Yuan et al. (2016), and implemented via the EMCEE sampler (Foreman-Mackey et al. 2013).

3.3. Empirical Characterization of the Luminosity Function Evolution with KDE

As a first step toward constructing a physically motivated parametric model for the SFG LF at low radio frequencies (150 MHz), we begin by applying the non-parametric KDE method (Section 3) to the ELAIS-N1 field—the deepest of the three fields in our sample. The high completeness and depth of this field allow for a ro-

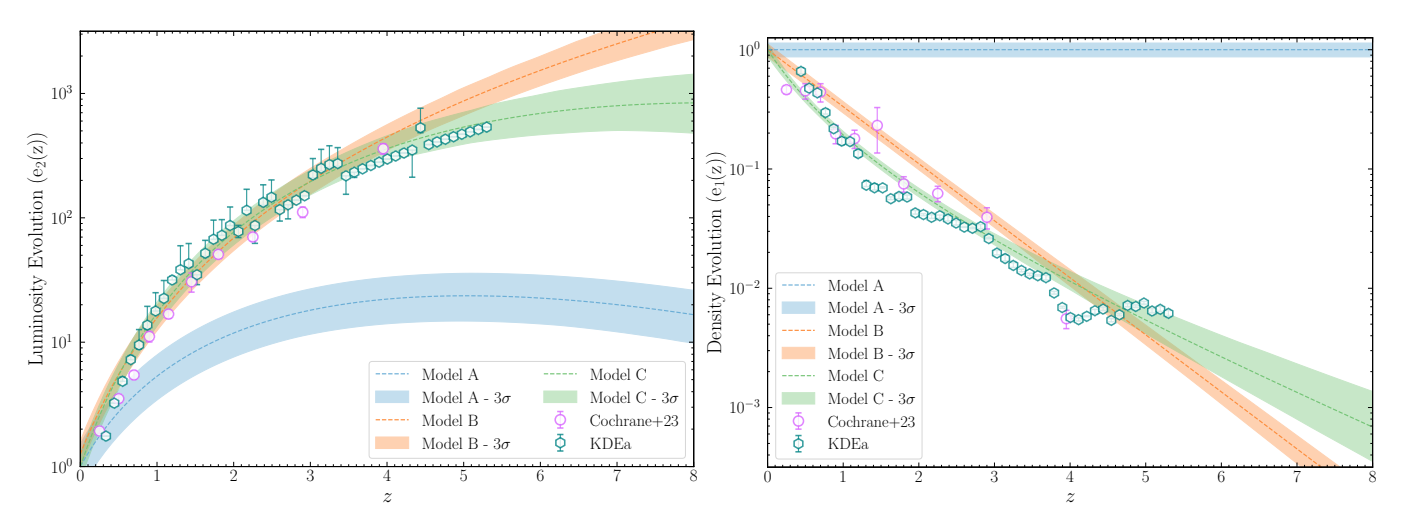


Figure 3. Redshift evolution of the luminosity (left) and comoving number density (right) of the reference points identified along the KDE-estimated LFs in the ELAIS-N1 field, shown as green hexagons. Assuming a redshift-invariant LF shape, the evolution of these reference points closely traces the underlying LADE trends. Colored curves represent the LE and DE functions derived from our three parametric LF models, with light shaded regions indicating their corresponding 3σ uncertainty intervals. Purple circles denote the estimates reported by Cochrane et al. (2023).

bust, data-driven reconstruction of the LF shape across a wide range of redshifts and luminosities.

This KDE-based estimate serves as an empirical reference for identifying key features of the LF, such as the location of the turnover, the slopes at the faint and bright ends, and possible redshift evolution patterns. Based on these insights, we then propose parametric models that capture the observed LF behavior and proceed to constrain their parameters using the likelihood framework introduced above.

In Figure 2, we present the LFs estimated at different redshifts using the adaptive KDE method. Specifically, the redshift range is discretized into a series of grid points, and the LF is computed at each of these redshift slices. The resulting curves are color-coded according to redshift, with the color bar in Figure 2 indicating the mapping between redshift and color.

As shown in Figure 2, the LF exhibits clear evolutionary trends with redshift. As redshift increases, the LF curves systematically shift toward higher luminosities along the horizontal axis. In addition, a systematic decrease in normalization is also observed, with the curves shifting downward along the vertical axis. This pattern suggests that typical SFGs tend to be more luminous at higher redshifts, while their comoving number density decreases over time—consistent with a scenario of LADE.

To quantitatively investigate the trends of density evolution (DE) and luminosity evolution (LE), we identify representative reference points along the KDE-estimated LF curves and track how these points evolve with redshift. Specifically, we compute the first deriva-

tive of $\phi_{\text{KDEa}}(z,L)$ with respect to $\log_{10}L$, and select the locations where the absolute value of the derivative reaches a minimum. These points, indicated by solid circles in Figure 2, correspond to the flattest regions of the $\phi_{\text{KDEa}}(z,L)$ curves—i.e., where the LF varies most slowly with luminosity. Their redshift evolution provides additional insight into the combined effects of LADE.

The evolution of these reference points with redshift is visualized in Figure 3, where we track their trajectories in both luminosity (horizontal axis) and comoving number density (vertical axis). This provides a quantitative means of disentangling the respective contributions of LADE to the overall LF evolution. Under the assumption that the shape of the LF remains invariant with redshift, the evolution of these reference points effectively captures the redshift dependence of the LADE functions. Specifically, horizontal shifts reflect luminosity evolution, while vertical displacements correspond to changes in comoving number density. As shown in Figure 3, the trajectories of the reference points reveal clear signatures of both luminosity and density evolution. This empirical evidence motivates the adoption of a mixed-evolution model, in which the LF is parameterized as a combination of redshift-dependent LADE terms.

3.4. Models for the Luminosity Function of Star-Forming Galaxies

Guided by the empirical trends revealed in the KDEbased analysis of the ELAIS-N1 field (Section 3.3), we now turn to constructing parametric models for the LF of SFGs. In particular, the observed simultaneous shift

in luminosity and normalization with increasing redshift strongly supports a scenario involving both LE and DE. The SFG LF can be expressed as

$$\Phi(z, L) = e_1(z) \,\phi(z = 0, L/e_2(z), \eta^j), \tag{15}$$

where $e_1(z)$ and $e_2(z)$ denote the redshift-dependent DE and LE functions, respectively, and η^j represents the parameters that define the shape of the LF. A constant η^j indicates that the LF shape remains invariant with redshift, while a redshift-dependent η^j implies luminosity-dependent density evolution (see Singal et al. 2013, 2014, for details). Consistent with many recent studies (e.g., Novak et al. 2017; van der Vlugt et al. 2022; Wang et al. 2024), we assume that the LF shape does not evolve with redshift, i.e., η^j is constant.

Following earlier work (e.g., Smolčić et al. 2009; Gruppioni et al. 2013; van der Vlugt et al. 2022; Wang et al. 2024), the local LF $\phi(z=0, L/e_2(z=0))$ is modeled using the modified Schechter function proposed by Saunders et al. (1990):

$$\phi(z=0, L/e_2(z=0)) = \frac{dN}{d\log_{10} L}$$

$$= \phi_{\star} \left(\frac{L}{L_{\star}}\right)^{1-\beta} \exp\left[-\frac{1}{2\gamma^2}\log^2\left(1 + \frac{L}{L_{\star}}\right)\right], \tag{16}$$

where L_{\star} , β , γ , and ϕ_{\star} are free parameters; L_{\star} marks the characteristic luminosity (or "knee") of the LF, β and γ control the slopes at the faint and bright ends, respectively, and ϕ_{\star} is the normalization constant.

To capture the observed redshift evolution, we consider three LF models, each adopting the same LE function:

$$e_2(z) = (1+z)^{k_1+k_2z},$$
 (17)

where k_1 and k_2 are free parameters. The DE function $e_1(z)$ differs among models:

• Model A assumes PLE, commonly used in the literature (e.g., Novak et al. 2017), with

$$e_1(z) = 1.$$
 (18)

 Model B introduces an exponential density evolution:

$$e_1(z) = 10^{p_1 z}, (19)$$

 Model C adopts a redshift-dependent power-law form:

$$e_1(z) = (1+z)^{p_1+p_2z},$$
 (20)

where p_1 and p_2 are additional free parameters. Models B and C represent the so-called "mixture evolution" or "LADE" scenarios, which allow for greater flexibility in modeling the joint evolution of number density and luminosity over cosmic time (e.g., Yuan et al. 2016, 2017; Aird et al. 2010). Unlike previous studies that fixed the local LF parameters to externally measured values (e.g. Cochrane et al. 2023), all parameters in Equation (16) are treated as free variables and are fitted simultaneously with the luminosity and density evolution parameters, using a MCMC approach implemented with the EMCEE Python package (Foreman-Mackey et al. 2013). This yields a fully self-consistent determination of both the local LF shape and its cosmic evolution.

3.5. Model Selection

To determine which of the proposed LF models (i.e., Models A–C in Section 3.4) provides the best description of the observed data, we apply model selection criteria based on information theory. These statistical tools quantify the trade-off between goodness of fit and model complexity, allowing for an objective comparison of models with different numbers of parameters.

Among them, the Akaike Information Criterion (AIC; Akaike 1974) is widely used and defined as

$$AIC = S_{\star}(\hat{\theta}) + 2q, \tag{21}$$

where S_{\star} is the total negative log-likelihood defined in Equation (13), $\hat{\theta}$ denotes the maximum-likelihood estimates of the model parameters, and q is the number of free parameters. The model with the lowest AIC value is considered the most favorable in terms of the balance between fit quality and parsimony.

We also consider the Bayesian Information Criterion (BIC; Schwarz 1978), which imposes a stronger penalty for model complexity:

$$BIC = S_{\star}(\hat{\theta}) + q \ln n, \tag{22}$$

where n is the total number of observed sources. Compared to AIC, BIC tends to prefer simpler models when the sample size is large. In our analysis, both AIC and BIC are used to assess the relative performance of Models A–C.

4. RESULTS

4.1. Luminosity Function Fitting for the the ELAIS-N1 field

Figure 4 presents the best-fitting LFs for the ELAIS-N1 field derived from Model A (blue solid line), Model B (orange solid line), and Model C (green solid line). All LFs are evaluated at the rest-frame frequency of

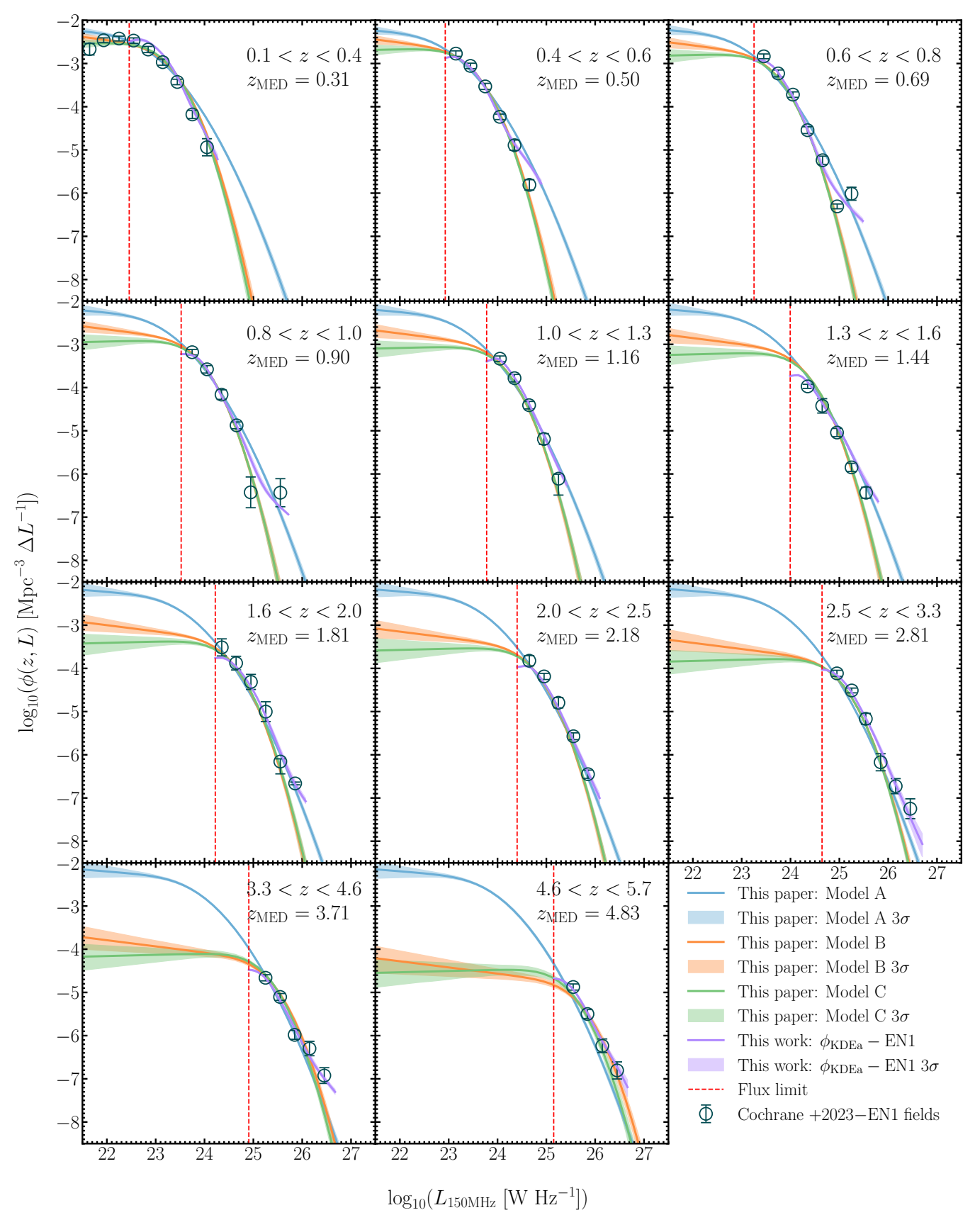


Figure 4. Radio LFs of SFGs in the ELAIS-N1 field at various redshifts. Blue, orange, and green solid lines show the best-fit LFs from Models A, B, and C, respectively. The light shaded area shows the 3σ confidence interval. The vertical red dashed line in each panel indicates the luminosity threshold corresponding to the survey flux limit at the given redshift. The solid purple lines indicate adaptive KDE LFs and shaded areas indicate 3σ confidence intervals. Circles with error bars denote the binned LF from Cochrane et al. (2023).

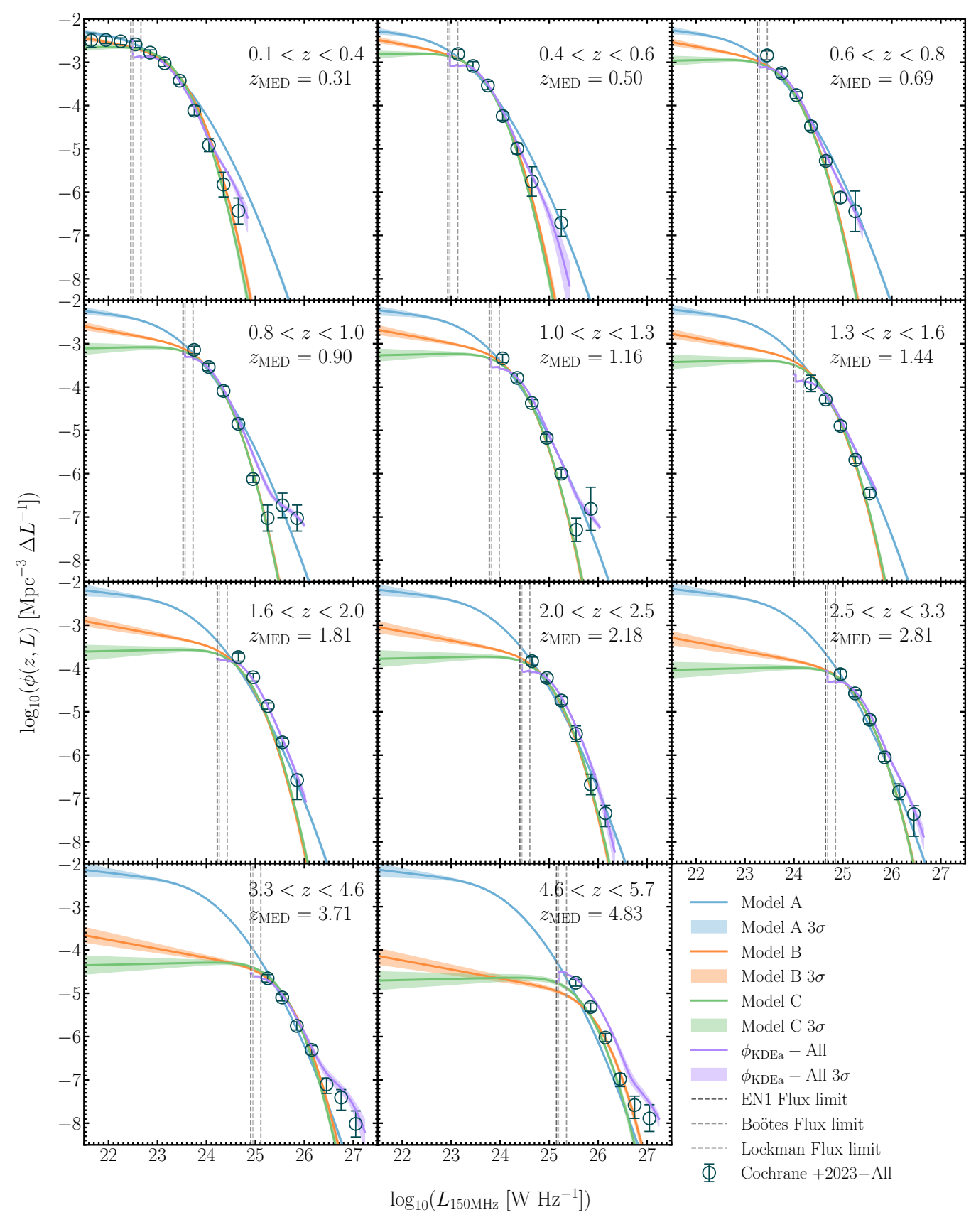


Figure 5. Similar to Figure 4, but for the combined analysis of all fields. The three dashed vertical lines in each panel indicate the luminosity thresholds corresponding to the survey flux limits of the ELAIS-N1, Boötes, and Lockman Hole fields at the given redshift.

Table 1. Best-fit parameters for the ELAIS-N1 field: Models A, B, and C

Model	$\log_{10}(\phi_{\star})$	$\log_{10}(L_{\star})$	β	γ	k_1	k_2	p_1	p_2
A	$-2.295^{+0.018}_{-0.018}$	$21.718^{+0.067}_{-0.061}$	$1.089^{+0.046}_{-0.041}$	$0.707^{+0.007}_{-0.007}$	$2.571^{+0.026}_{-0.026}$	$-0.162^{+0.005}_{-0.005}$		
В	$-2.423^{+0.018}_{-0.018}$	$22.283^{+0.036}_{-0.036}$	$1.142^{+0.029}_{-0.026}$	$0.427^{+0.007}_{-0.008}$	$3.640^{+0.029}_{-0.029}$	$0.002^{+0.007}_{-0.007}$	$-0.478^{+0.007}_{-0.007}$	
С	$-2.237^{+0.019}_{-0.019}$	$22.214^{+0.039}_{-0.035}$	$0.970^{+0.037}_{-0.032}$	$0.421^{+0.006}_{-0.006}$	$4.247^{+0.059}_{-0.059}$	$-0.148^{+0.015}_{-0.015}$	$-2.239^{+0.083}_{-0.083}$	$-0.135^{+0.021}_{-0.021}$

Note. Units — ϕ_{\star} : [Mpc⁻³ dex⁻¹], L_{\star} : [W Hz⁻¹]. The best-fit parameters as well as their 1σ errors for models A, B, and C.

Table 2. Best-fit parameters for All fields: Models A, B, and C

Model	$\log_{10}(\phi_{\star})$	$\log_{10}(L_{\star})$	β	γ	k_1	k_2	p_1	p_2
A	$-2.381^{+0.013}_{-0.013}$	$21.784^{+0.045}_{-0.040}$	$1.135^{+0.031}_{-0.028}$	$0.703^{+0.004}_{-0.004}$	$2.791^{+0.017}_{-0.017}$	$-0.186^{+0.003}_{-0.003}$		• • •
В	$-2.604^{+0.013}_{-0.013}$	$22.555^{+0.022}_{-0.022}$	$1.209^{+0.016}_{-0.016}$	$0.384^{+0.005}_{-0.005}$	$3.914^{+0.020}_{-0.020}$	$-0.034^{+0.005}_{-0.005}$	$-0.487^{+0.004}_{-0.004}$	
С	$-2.324^{+0.013}_{-0.013}$	$22.312^{+0.024}_{-0.024}$	$0.974^{+0.023}_{-0.023}$	$0.382^{+0.004}_{-0.004}$	$4.670^{-0.033}_{-0.033}$	$-0.204^{+0.007}_{-0.007}$	$-2.536^{+0.047}_{-0.047}$	$-0.094^{+0.011}_{-0.011}$

Note. Units $-\phi_{\star}$: [Mpc⁻³ dex⁻¹], L_{\star} : [W Hz⁻¹]. The best-fit parameters as well as their 1σ errors for models A, B, and C.

150 MHz. For comparison, we also include the binned LFs from Cochrane et al. (2023), shown as blue circles with error bars. The KDE-based non-parametric estimates are shown as purple solid lines, with the shaded regions indicating the 3σ confidence intervals, and are in good agreement with the binned LFs from Cochrane et al. (2023).

For the ELAIS-N1 field, the marginalized one- and two-dimensional posterior distributions of the model parameters are shown in Figures 9, 10, and 11 for Models A, B, and C, respectively. These corner plots demonstrate that all parameters are well constrained across the three models. Table 1 summarizes the best-fitting parameter values and their 1σ uncertainties for the ELAIS-N1 field.

Notably, both the binned LFs from Cochrane et al. (2023) and our KDE-based non-parametric estimates exhibit a distinct bump at the high-luminosity end. Because the non-parametric estimates are entirely datadriven, this excess directly reflects the structure of the observed sample rather than assumptions in the modeling. When compared with the best-fitting parametric LFs, the non-parametric estimates show systematically higher number densities at the bright end, indicating that the excess arises relative to the model predictions. While low-number statistics could in principle contribute to this feature, it is unlikely to be the dominant factor, as a similar bright-end excess is seen across nearly all redshift bins in Figure 4. To assess the possible influence of these sparse data points, we repeated the parametric fitting after excluding the highest-luminosity bin in each redshift interval—typically containing only one or two sources. The resulting best-fit parameters and evolutionary trends changed negligibly, confirming that our conclusions are robust against the inclusion of these bins. A plausible explanation for this feature is the contamination from misclassified sources: although our sample is selected to represent SFGs, it is likely that some AGNs remain unidentified and contribute disproportionately at high luminosities. The presence of such AGNs would elevate the number density in the bright end, thereby producing the observed bump.

In each panel of Figure 4, we indicate the luminosity threshold corresponding to the survey flux limit of the ELAIS-N1 field at the given redshift by a vertical red dashed line. Above this threshold, Models B and C yield nearly identical results and show good agreement with both the binned LFs and the KDE-based estimates. Model A, in contrast, exhibits a slightly shallower decline at the bright end, deviating mildly from the other two models. This behavior appears to reflect a stronger response to the mild upturn observed at the high-luminosity end of the binned and KDE-based LFs—possibly caused by residual AGN contamination—suggesting that Model A may be overfitting to this bright-end feature.

Below the luminosity threshold, the three models begin to diverge more significantly. Since this regime lies beyond the reach of the observed data, comparisons with the binned LFs or KDE estimates are not feasible. In such extrapolated domains, statistical model selection criteria become essential for assessing model performance. To this end, we employ the AIC and the BIC both of which balance goodness-of-fit against model complexity. Table 3 presents the AIC and BIC values for Models A, B, and C in the ELAIS-N1 field. Model C yields the lowest values in both criteria, followed closely by Model B, while Model A is strongly disfavored.

To highlight the relative performance, we also compute ΔAIC and ΔBIC with respect to the best-

Table 3. Model comparison based on AIC and BIC for the ELAIS-N1 field. Δ AIC and Δ BIC are computed relative to the model with the minimum value.

Model	AIC	$\Delta { m AIC}$	BIC	$\Delta \mathrm{BIC}$
A	387621.2	1709.8	387669.1	1693.8
В	386020.7	109.3	386076.6	101.3
С	385911.4	0.0	385975.3	0.0

Table 4. AIC and BIC values for all fields: Models A, B, and C. Differences Δ AIC and Δ BIC are calculated relative to the best-performing model (Model B).

Model	AIC	$\Delta { m AIC}$	BIC	$\Delta \mathrm{BIC}$
A	1038437.2	15020.3	1038490.9	15011.4
В	1023417.0	0.0	1023479.5	0.0
\mathbf{C}	1028178.9	4761.9	1028250.4	4770.9

performing model. A difference larger than 10 is typically interpreted as strong evidence against a model. In our case, not only is Model A clearly ruled out, but Model C is also decisively preferred over Model B. Model B also performs significantly better than Model A, suggesting that incorporating some form of density evolution improves the model fit. These results support the adoption of a mixed-evolution scenario—combining both luminosity and density evolution—as the most appropriate framework for modeling the SFG LF in the ELAIS-N1 field.

In addition to the statistical model comparisons, we also examine how well the fitted evolution trends from Models A, B, and C reproduce the non-parametric estimates of LADE obtained from the KDE analysis. As shown in Figure 3, Model C provides the closest match to the KDE-derived LE and DE trends, while Model B also shows broadly consistent behavior within uncertainties. In contrast, Model A deviates more noticeably, particularly in the density evolution component. This consistency between the non-parametric and parametric results provides further support for adopting a mixed-evolution framework when modeling the SFG LF.

4.2. Luminosity Function Fitting for the Combined Sample

To further constrain the SFG LF, we combine the data from the three fields—ELAIS-N1, Boötes, and Lockman Hole—into a unified sample and apply the same modeling framework as in the individual field analysis. The best-fitting LFs obtained using Models A, B, and C are compared against the averaged KDE-based non-parametric estimates derived from the individual fields. The marginalized posterior distributions for Models A,

B, and C in the combined analysis are presented in Figures 12, 13, and 14, respectively, showing that all model parameters are well constrained. The corresponding best-fitting values and their 1σ uncertainties are summarized in Table 2.

Figure 5 presents the resulting LFs from the combined analysis. The best-fit LFs for Models A (blue), B (orange), and C (green) are shown in each redshift bin, alongside the binned estimates from Cochrane et al. (2023) and the averaged KDE results (purple solid lines with 3σ confidence intervals). The three vertical dashed lines in each panel indicate the luminosity thresholds corresponding to the survey flux limits of the ELAIS-N1, Boötes, and Lockman Hole fields at the given redshift. As in the ELAIS-N1 field, both the binned and KDE LFs exhibit a mild bright-end excess across redshift bins, potentially due to residual AGN contamination. The overall behavior of the three parametric models resembles that observed in the ELAIS-N1 field: they agree above the luminosity thresholds, while more substantial differences emerge at the faint end, where observational constraints are absent.

Figure 5 presents the resulting LFs from the combined analysis. The best-fit LFs for Models A (blue), B (orange), and C (green) are shown in each redshift bin, alongside the binned estimates from Cochrane et al. (2023) and the averaged KDE results (purple solid lines with 3σ confidence intervals). Overall, the KDE LFs are in good agreement with the binned estimates of Cochrane et al. (2023) across most redshift bins. However, at the highest redshift interval (4.6 < z < 5.7), a noticeable deviation appears. This arises partly because the original KDE formalism (Yuan et al. 2022) is designed for a single flux-limited sample and cannot directly account for multiple surveys with different flux limits. In our implementation, we therefore compute the KDE LFs separately for the three fields and take their average as an approximate combined estimate. While this provides a practical compromise, it inevitably introduces additional uncertainty at the high-redshift, highluminosity end, where the data are sparse. The three vertical dashed lines in each panel indicate the luminosity thresholds corresponding to the survey flux limits of the ELAIS-N1, Boötes, and Lockman Hole fields at the given redshift. As in the ELAIS-N1 field, both the binned and KDE LFs exhibit a mild bright-end excess across redshift bins, potentially due to residual AGN contamination. The overall behavior of the three parametric models resembles that observed in the ELAIS-N1 field: they agree above the luminosity thresholds, while more substantial differences emerge at the faint end, where observational constraints are absent.

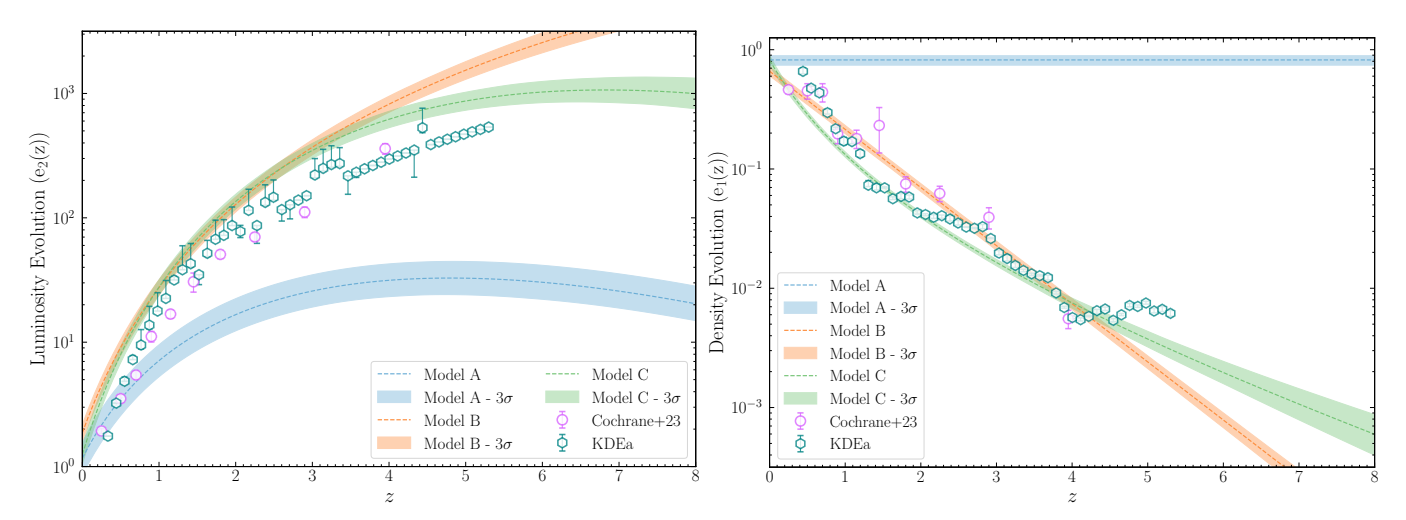


Figure 6. LE and DE fitted from our three parametric LF models using the combined sample of all fields, with light shaded regions indicating the corresponding 3σ uncertainty intervals. The green hexagons and purple circles represent the LE and DE trends based solely on the ELAIS-N1 field (same as in Figure 3).

Figure 6 shows the fitted LE and DE functions from Models A, B, and C using the combined dataset, overlaid with the KDE-derived LE and DE trends (green hexagons, same as Figure 3) based solely on the ELAIS-N1 field. For Models B and C, the fitted LE and DE functions broadly reproduce the KDE-derived evolutionary trends, although the LE curves rise more steeply and the DE curves decline more rapidly than those inferred from the ELAIS-N1 field alone. Interestingly, this behavior reveals a possible "see-saw" degeneracy between LE and DE: when LE evolves more strongly with redshift, DE tends to decrease more steeply, and vice versa. This degeneracy likely reflects the intrinsic trade-off between LE and DE in modeling the redshift-luminosity distribution of SFGs.

Table 4 summarizes the AIC and BIC values for the three models. The Δ AIC and Δ BIC values are computed relative to the best-performing model, Model B. The results show that Model A, which assumes PLE, is strongly disfavored. Although Model C provides greater flexibility through an additional density evolution parameter, it does not outperform the simpler Model B in the joint analysis. These findings reinforce the importance of including density evolution in modeling the SFG LF, while also highlighting the balance between model complexity and data support: a simpler mixed-evolution model (Model B) offers the best overall fit when all fields are considered.

Interestingly, while Model C is statistically preferred in the ELAIS-N1 field, the combined analysis across all three fields identifies Model B as the optimal model based on both AIC and BIC. This shift can be understood in terms of the trade-off between model complexity and generalizability. The additional degree of

freedom in Model C may provide improved flexibility in fitting detailed LF features in deep fields such as ELAIS-N1, which probe wider luminosity and redshift ranges. However, when applied to the combined dataset—including the shallower Boötes and Lockman Hole fields—this flexibility offers diminishing returns, as these two fields do not significantly extend the luminosity coverage nor enhance constraints near the LF knee where model differences are most evident.

Although the inclusion of multiple fields increases the total number of sources, it does not necessarily improve constraints on the critical regions of the LF. Instead, the shallow fields primarily contribute data in luminosity ranges where all models already converge, while still increasing the penalty term in AIC and BIC due to added complexity. Consequently, the statistical advantage of Model C becomes diluted, and the simpler Model B emerges as the more robust and generalizable choice for the full sample.

These results emphasize an important methodological consideration: combining datasets with varying depths and flux limits is only beneficial when the added fields offer complementary constraints. In this study, the Boötes and Lockman Hole fields do not augment the high-luminosity end or better constrain the turnover of the LF; hence, their inclusion does not enhance model discrimination and may even obscure subtle evolutionary features detectable in the deeper ELAIS-N1 field.

In summary, Model C provides the best fit to the deepest field, capturing more detailed redshift evolution features, but Model B delivers a more parsimonious and statistically favored description when all fields are considered. We thus conclude that while Model C may be preferable in deep-field studies with extensive redshift

coverage, Model B offers greater stability and generalizability across heterogeneous survey conditions.

4.3. Comparing ELAIS-N1 and Combined Fields: Role of External Constraints

To evaluate the impact of the additional constraints introduced in Equation (13), we now examine how the best-fit models reproduce the observed LRLF and Euclidean-normalized SCs. We note that the observed LRLF and source counts were also included as constraints in the fitting procedure (see Section 3). Therefore, the comparisons presented here should not be regarded as independent tests, but rather as consistency checks to illustrate how well the fitted models reproduce the basic observational quantities on which they are based.

Figure 7 provides a direct comparison between the modeled and observed LRLFs at 150 MHz for both the ELAIS-N1 field (left panel) and the combined sample of all fields (right panel). In both cases, the rightpointing triangles represent the binned LRLF measurements from Cochrane et al. (2023), while the colored curves show the best-fit predictions from Models A (blue), B (orange), and C (green). Models B and C show excellent agreement with the observed LRLF in the range $L \lesssim 10^{24} \,\mathrm{W\,Hz^{-1}}$. However, in the two highestluminosity bins, the binned LRLF shows a noticeable excess that is not captured by Models B or C. This feature likely reflects residual AGN contamination, or the presence of galaxies exhibiting a coexistence of AGN activity and star formation. Such hybrid systems—where both star formation and AGN contribute significantly to the radio emission—are known to be common in the intermediate-to-high luminosity regime, particularly in composite galaxies or systems hosting low-excitation radio AGN (e.g., Mingo et al. 2014; Dicken et al. 2012; Delvecchio et al. 2017; Gürkan et al. 2018). Model A, which predicts a shallower decline at the bright end, appears to overfit the observed excess in an attempt to accommodate it. However, this results in a poorer overall fit across the full luminosity range.

Figure 8 presents a comparison between the observed and modeled Euclidean-normalized radio SCs. The left panel corresponds to the ELAIS-N1 field, while the right panel shows results from the combined dataset of all three fields. In both panels, the purple circles represent the binned counts derived from the LOFAR flux density distributions using the binning method, and the colored lines indicate the predictions from our three parametric models. The blue solid, orange dash-dotted, and green dashed lines correspond to Models A, B, and C,

respectively. Shaded regions indicate the 3σ confidence intervals.

Models B and C reproduce the observed SCs well over a wide range of flux densities, for both the ELAIS-N1 field and the full combined sample. In contrast, Model A shows substantial deviations across the entire flux range, highlighting its overall poorer agreement with the observed SCs. It is also worth noting that at the bright end $(F_{\nu} \gtrsim 10 \,\mathrm{mJy})$, the increased scatter in the binned SCs likely arises from a combination of Poisson noise and classification uncertainties. In this regime, the separation between SFGs and AGNs becomes increasingly ambiguous: some AGNs may be misclassified as SFGs, while certain high-luminosity SFGs exhibiting AGN-like features might be incorrectly excluded. This dual source of contamination, combined with low-number statistics, makes the bright-end flux range particularly challenging to model reliably. In addition, at the faint end, the binned SCs drop significantly below the model predictions. This underestimation likely arises from completeness issues near the flux limit in the three fields, where faint sources are more easily missed, leading to a downward bias in the SCs.

In summary, both Model B and Model C consistently reproduce the observed LRLF and Euclidean-normalized SCs. Their success in matching the observational data demonstrates the robustness and flexibility of the mixed-evolution framework in capturing the redshift and luminosity trends of SFGs. In contrast, Model A, which assumes pure luminosity evolution, fails to provide an adequate fit to either constraint. These results further support the conclusion that incorporating density evolution is essential for accurately modeling the radio LF of SFGs.

5. DISCUSSION AND CONCLUSIONS

We have developed a non-parametric framework for characterizing the evolution of the 150 MHz luminosity function (LF) of star-forming galaxies (SFGs). By applying kernel density estimation (KDE) in the luminosity—redshift plane, we reconstruct a smooth estimate of the joint source distribution that enables evaluation of the LF at arbitrary redshifts, without the need for binning or a predefined analytic form.

Building on this non-parametric foundation, we examine the LF evolution by tracking the displacement of key reference points along the KDE-derived curves, providing a direct, data-driven view of luminosity and density evolution (LADE). These empirical trends then serve as guidance for constructing parametric models, which are fitted using a global maximum-likelihood approach. This combination links the empirical flexibility

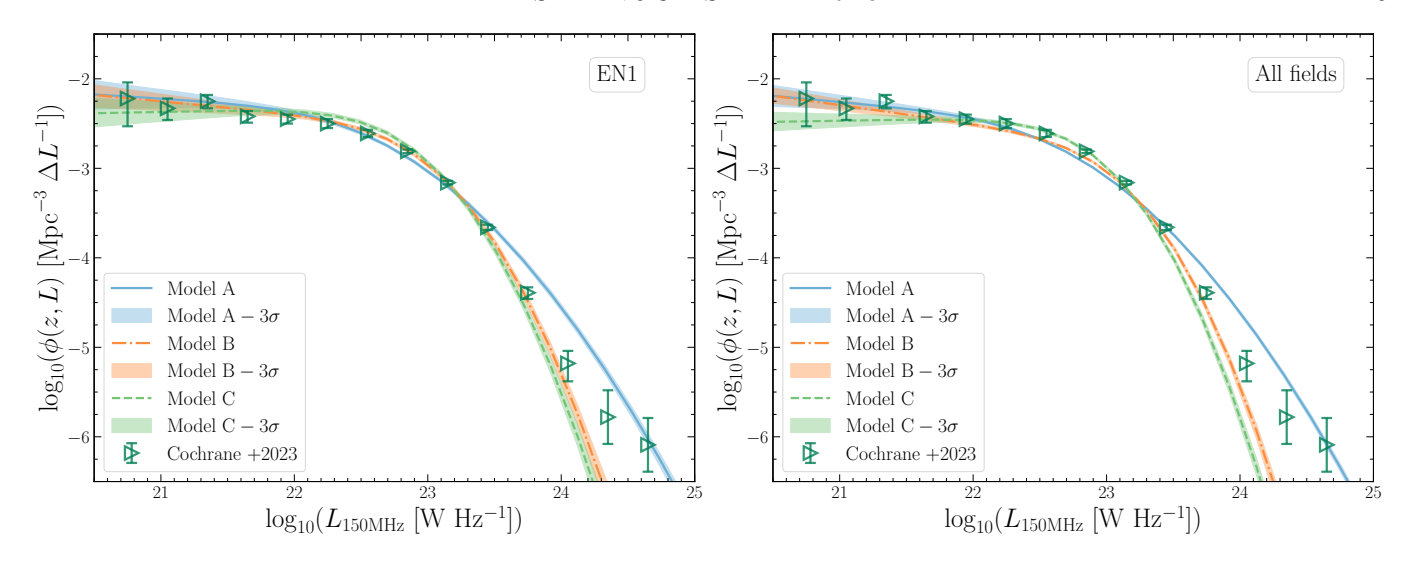


Figure 7. Local radio LF at 150 MHz of SFGs for the ELAIS-N1 field (*left*) and the combined sample of all fields (*right*). In both panels, the right-pointing triangles with error bars represent the binned LRLF measurements from Cochrane et al. (2023), while the colored curves show the corresponding best-fit model predictions from this work.

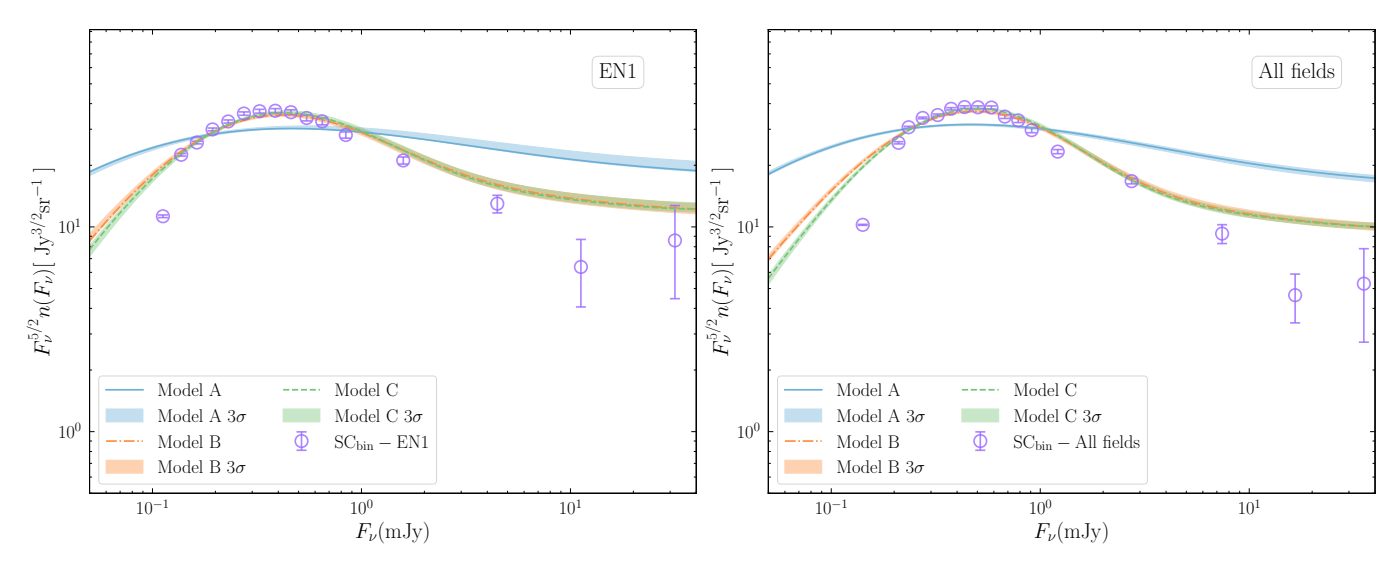


Figure 8. Comparison of our best-fit models with the SCs obtained using the binned method in the ELAIS-N1 field (left panel) and combined all three fields (right panel). In both panels, the blue solid line, orange dashed-dotted line, and green dashed line represent the best-fit SCs for Models A, B, and C, respectively. The purple circles denote the SCs obtained using the bin method.

of KDE with the statistical rigor of parametric inference, providing a unified view of the evolving radio SFG population.

The evolution of the LF has also been studied in Cochrane et al. (2023) using deep 150 MHz data from the Low Frequency Array (LOFAR) Two-metre Sky Survey (LoTSS). In their analysis, the redshift dependence of the LF parameters was derived by dividing the sample into redshift bins and constructing binned LFs with the $1/V_{\rm max}$ method. These LF points were then fitted with a parametric form matching the locally derived LF, with the faint-end slope α and high-luminosity cut-off σ

fixed, while L_* and ϕ_* were allowed to vary. This yielded a pair of (L_*, ϕ_*) values per redshift slice, forming the basis of their evolutionary trends.

Our parametric modeling follows the same general assumption as Cochrane et al. (2023), namely that the LF shape is fixed with redshift and the evolution is captured through changes in L_* and ϕ_* . The main difference lies in how these trends are inferred: rather than fitting (L_*, ϕ_*) independently in redshift bins, we perform a global maximum-likelihood fit across all fields and redshifts, guided by the non-parametric KDE results.

In this context, our analysis extends the methodology of Cochrane et al. (2023) by integrating non-parametric reconstruction and parametric modeling into a single, data-driven framework. This reduces sensitivity to binning choices and allows continuous evolution to emerge directly from the data. The main findings of this work are summarized below.

- 1. The KDE analysis reveals clear empirical evidence for simultaneous luminosity and density evolution (LADE): the LF systematically shifts toward higher luminosities and lower normalizations with increasing redshift.
- 2. Guided by the KDE trends, we developed three parametric LF models: Model A (pure luminosity evolution, PLE), and Models B and C (both LADE forms differing in their density evolution). These models were fitted using a global maximum-likelihood framework that incorporates completeness corrections and observational constraints from the local LF and Euclidean-normalized source counts.
- 3. Models B and C successfully reproduce the observed LFs and source counts across a broad luminosity and flux range, confirming the need for models including density evolution. Model A performs significantly worse, highlighting the limitations of pure luminosity evolution. Model C provides the best fit for the deepest field (ELAIS-N1), while the simpler Model B yields the most statistically favored and stable results in the combined-field analysis.
- 4. A mild excess persists at the bright end of the LF across different estimators (binned and KDE). This feature likely reflects residual active galactic nuclei (AGN) contamination rather than a genuine SFG population, emphasizing the need for improved AGN/SFG separation in future radio surveys.

5. The combined use of non-parametric KDE and parametric maximum-likelihood modeling offers a flexible and statistically robust framework for tracing the cosmic evolution of radio-selected SFGs. With future surveys such as the Square Kilometre Array (SKA) vastly expanding the accessible ranges in luminosity and redshift, this approach will be essential for fully exploiting the scientific potential of next-generation radio observations.

We thank the anonymous reviewer for the many constructive comments and suggestions, leading to a clearer description of these results. We acknowledge financial support from the Science Fund for Distinguished Young Scholars of Hunan Province (Grant No. 2024JJ2040), the National Natural Science Foundation of China (Grant Nos. 12073069, 12075084, 12275080, and 12393813), the Major Basic Research Project of Hunan Province (Grant No. 2024JC0001), and the Innovative Research Group of Hunan Province (Grant No. 2024JJ1006). Z.Y. is supported by the Xiaoxiang Scholars Programme of Hunan Normal University. We thank R. K. Cochrane for insightful discussions and valuable guidance on the data classification process. LOFAR data products were provided by the LOFAR Surveys Key Science project (LSKSP; https://lofarsurveys.org/) and were derived from observations with the International LOFAR Telescope (ILT). LOFAR (van Haarlem et al. 2013) is the Low Frequency Array designed and constructed by ASTRON. It has observing, data processing, and data storage facilities in several countries, which are owned by various parties (each with their own funding sources), and which are collectively operated by the ILT foundation under a joint scientific policy. The efforts of the LSKSP have benefited from funding from the European Research Council, NOVA, NWO, CNRS-INSU, the SURF Co-operative, the UK Science and Technology Funding Council and the Jülich Supercomputing Centre.

REFERENCES

Aird, J., Coil, A. L., & Georgakakis, A. 2017, MNRAS, 465, 3390, doi: 10.1093/mnras/stw2932

Aird, J., Nandra, K., Laird, E. S., et al. 2010, MNRAS, 401, 2531, doi: 10.1111/j.1365-2966.2009.15829.x

Akaike, H. 1974, IEEE Transactions on Automatic Control, 19, 716

Algera, H. S. B., van der Vlugt, D., Hodge, J. A., et al. 2020, ApJ, 903, 139, doi: 10.3847/1538-4357/abb77a Ashby, M. L., Stern, D., Brodwin, M., et al. 2009, ApJ, 701, 428, doi: 10.1088/0004-637X/701/1/428

Bell, E. F. 2003, ApJ, 586, 794, doi: 10.1086/367829

Best, P. N., Kondapally, R., Williams, W., et al. 2023, MNRAS, doi: 10.1051/0004-6361/202038828

Bouwens, R. J., Illingworth, G. D., Oesch, P. A., et al. 2015, ApJ, 803, 34, doi: 10.1088/0004-637X/803/1/34

- Bouwens, R. J., Oesch, P. A., Stefanon, M., et al. 2021, AJ, 162, 47, doi: 10.3847/1538-3881/abf83e
- Calistro Rivera, G., Williams, W. L., Hardcastle, M. J., et al. 2017, MNRAS, 469, 3468, doi: 10.1093/mnras/stx1040
- Chambers, K. C., Magnier, E. A., Metcalfe, N., et al. 2016, arXiv e-prints, arXiv:1612.05560. https://arxiv.org/abs/1612.05560
- Chen, Y.-C. 2017, Biostatistics & Epidemiology, 1, 161Cochrane, R. K., Kondapally, R., Best, P. N., et al. 2023,MNRAS, 523, 6082, doi: 10.1093/mnras/stad1602
- Condon, J. J., Anderson, M. L., & Helou, G. 1991, ApJ, 376, 95, doi: 10.1086/170258
- Davies, T. M., & Baddeley, A. 2018, Statistics and Computing, 28, 937
- Delvecchio, I., Smolčić, V., Zamorani, G., et al. 2017, A&A, 602, A3, doi: 10.1051/0004-6361/201629367
- Dicken, D., Tadhunter, C., Axon, D., et al. 2012, ApJ, 745, 172, doi: 10.1088/0004-637X/745/2/172
- Drake, A. B., Simpson, C., Collins, C. A., et al. 2013, MNRAS, 433, 796, doi: 10.1093/mnras/stt775
- Duncan, K. J., Kondapally, R., Brown, M. J., et al. 2021, A&A, 648, A4, doi: 10.1051/0004-6361/202038809
- Enia, A., Talia, M., Pozzi, F., et al. 2022, ApJ, 927, 204, doi: 10.3847/1538-4357/ac51ca
- Fan, X., Strauss, M. A., Schneider, D. P., et al. 2001, The Astronomical Journal, 121, 54
- Foreman-Mackey, D., Hogg, D. W., Lang, D., & Goodman, J. 2013, Publications of the Astronomical Society of the Pacific, 125, 306
- Gonzalez, A. H. 2010, American Astronomical Society Meeting Abstracts 216
- Gruppioni, C., Pozzi, F., Rodighiero, G., et al. 2013, MNRAS, 432, 23, doi: 10.1093/mnras/stt308
- Gruppioni, C., Béthermin, M., Loiacono, F., et al. 2020, A&A, 643, A8, doi: 10.1051/0004-6361/202038487
- Gürkan, G., Hardcastle, M. J., Smith, D. J. B., et al. 2018, MNRAS, 475, 3010, doi: 10.1093/mnras/sty016
- Haarsma, D. B., Partridge, R. B., Windhorst, R. A., & Richards, E. A. 2000, ApJ, 544, 641, doi: 10.1086/317225
- Hogg, D. W. 1999, arXiv preprint astro-ph/9905116
- Ishigaki, M., Kawamata, R., Ouchi, M., et al. 2018, ApJ, 854, 73, doi: 10.3847/1538-4357/aaa544
- Kennicutt Jr, R. C. 1998, Annual Review of Astronomy and Astrophysics, 36, 189
- Kondapally, R., Best, P. N., Hardcastle, M. J., et al. 2021, A&A, 648, A3, doi: 10.1051/0004-6361/202038813
- Lawrence, A., Warren, S. J., Almaini, O., et al. 2007, MNRAS, 379, 1599,
 - doi: 10.1111/j.1365-2966.2007.12040.x

- Lonsdale, C. J., Smith, H. E., Robinson, M. R., et al. 2003, PASP, 115, 897
- Madau, P., & Dickinson, M. 2014, ARA&A, 52, 415, doi: 10.1146/annurev-astro-081811-125615
- Madau, P., Ferguson, H. C., Dickinson, M. E., et al. 1996, MNRAS, 283, 1388, doi: 10.1093/mnras/283.4.1388
- Magnelli, B., Ivison, R., Lutz, D., et al. 2015, Astronomy & Astrophysics, 573, A45
- Malefahlo, E. D., Jarvis, M. J., Santos, M. G., et al. 2022, MNRAS, 509, 4291, doi: 10.1093/mnras/stab3242
- Marshall, H., Tananbaum, H., Avni, Y., & Zamorani, G. 1983, The Astrophysical Journal, 269, 35
- Martin, D. C., Fanson, J., Schiminovich, D., et al. 2005, ApJ, 619, L1
- McLeod, D. J., McLure, R. J., & Dunlop, J. S. 2016, MNRAS, 459, 3812, doi: 10.1093/mnras/stw904
- McLure, R. J., Dunlop, J. S., Bowler, R. A. A., et al. 2013, MNRAS, 432, 2696, doi: 10.1093/mnras/stt627
- Mingo, B., Hardcastle, M. J., Croston, J. H., et al. 2014, MNRAS, 440, 269, doi: 10.1093/mnras/stu263
- Mohan, N., & Rafferty, D. 2015, Astrophysics Source Code Library. ascl:1502.007
- Novak, M., Smolčić, V., Delhaize, J., et al. 2017, A&A, 602, A5, doi: 10.1051/0004-6361/201629436
- Ocran, E., Taylor, A., Vaccari, M., et al. 2020, Monthly Notices of the Royal Astronomical Society, 491, 5911
- Ocran, E. F., Taylor, A. R., Vaccari, M., et al. 2020, MNRAS, 491, 5911, doi: 10.1093/mnras/stz3401
- Oesch, P. A., Bouwens, R. J., Illingworth, G. D., Labbé, I., & Stefanon, M. 2018, ApJ, 855, 105, doi: 10.3847/1538-4357/aab03f
- Oliver, S. J., Bock, J., Altieri, B., et al. 2012, MNRAS, 424, 1614, doi: 10.1111/j.1365-2966.2012.20912.x
- Ouchi, M., Shimasaku, K., Furusawa, H., et al. 2010, ApJ, 723, 869, doi: 10.1088/0004-637X/723/1/869
- Padovani, P. 2016, Astronomy and Astrophysics Review, 24, 13, doi: 10.1007/s00159-016-0098-6
- Pritchard, J., & Loeb, A. 2010, Nature, 468, 772, doi: 10.1038/468772b
- Riechers, D. A., Bradford, C. M., Clements, D. L., et al. 2013, Nature, 496, 329, doi: 10.1038/nature12050
- Rowan-Robinson, M., Oliver, S., Wang, L., et al. 2016, MNRAS, 461, 1100, doi: 10.1093/mnras/stw1169
- Sabater, J., Best, P. N., Tasse, C., et al. 2021, A&A, 648, A2, doi: 10.1051/0004-6361/202038828
- Sadler, E. M., Jenkins, C. R., & Kotanyi, C. G. 1989, MNRAS, 240, 591, doi: 10.1093/mnras/240.3.591
- Saunders, W., Rowan-Robinson, M., Lawrence, A., et al. 1990, Monthly Notices of the Royal Astronomical Society, 242, 318

Schmidt, M. 1968, ApJ, 151, 393, doi: 10.1086/149446
Schober, J., Schleicher, D. R. G., & Klessen, R. S. 2015, MNRAS, 446, 2, doi: 10.1093/mnras/stu1999

- Schwarz, G. 1978, The Annals of Statistics, 6, 461 , doi: 10.1214/aos/1176344136
- Singal, J., Ko, A., & Petrosian, V. 2014, The Astrophysical Journal, 786, 109
- Singal, J., Petrosian, V., Lawrence, A., et al. 2013, The Astrophysical Journal, 764, 43
- Smail, I., Ivison, R. J., & Blain, A. W. 1997, ApJL, 490, L5, doi: 10.1086/311017
- Smith, D. J. B., Haskell, P., Gürkan, G., et al. 2021, A&A, 648, A6, doi: 10.1051/0004-6361/202039343
- Smolčić, V., Zamorani, G., Schinnerer, E., et al. 2009, The Astrophysical Journal, 696, 24
- Smolčić, V., Schinnerer, E., Zamorani, G., et al. 2009, ApJ, 690, 610, doi: 10.1088/0004-637X/690/1/610
- Tabatabaei, F. S., Schinnerer, E., Krause, M., et al. 2017, ApJ, 836, 185, doi: 10.3847/1538-4357/836/2/185
- Tasse, C., Shimwell, T., Hardcastle, M. J., et al. 2021, A&A, 648, A1, doi: 10.1051/0004-6361/202038804

- van der Vlugt, D., Hodge, J. A., Algera, H. S. B., et al. 2022, ApJ, 941, 10, doi: 10.3847/1538-4357/ac99db
- Wang, W., Yuan, Z., Yu, H., & Mao, J. 2024, A&A, 683, A174, doi: 10.1051/0004-6361/202347746
- Wasserman, L. 2006, All of nonparametric statistics (Springer Science & Business Media)
- Weymann, R., Storrie-Lombardi, L., Sawicki, M., & Brunner, R., eds. 1999, Astronomical Society of the Pacific Conference Series, Vol. 191, Photometric Redshifts and the Detection of High Redshift Galaxies
- Willott, C. J., Rawlings, S., Blundell, K. M., Lacy, M., & Eales, S. A. 2001, Monthly Notices of the Royal Astronomical Society, 322, 536
- Yuan, Z., Jarvis, M. J., & Wang, J. 2020, The Astrophysical Journal Supplement Series, 248, 1
- Yuan, Z., Wang, J., Zhou, M., & Mao, J. 2016, The Astrophysical Journal, 820, 65
- Yuan, Z., Wang, J., Zhou, M., Qin, L., & Mao, J. 2017, The Astrophysical Journal, 846, 78
- Yuan, Z., Zhang, X., Wang, J., Cheng, X., & Wang, W. 2022, The Astrophysical Journal Supplement Series, 260, 10

APPENDIX

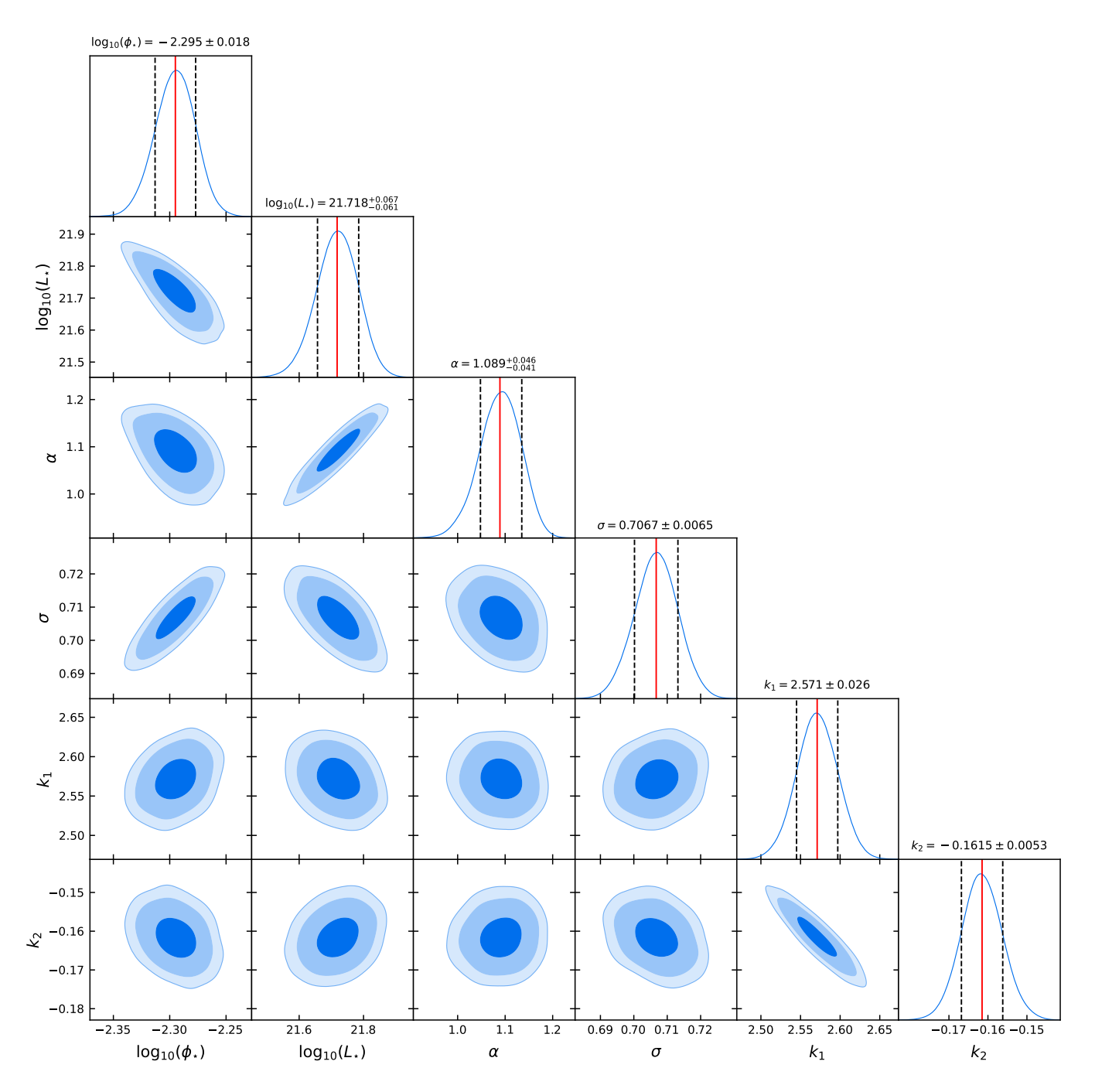


Figure 9. ELAIS-N1 field corner plot illustrating the one- and two-dimensional projections of the posterior probability distributions for Model A, derived from the MCMC sampling. The diagonal panels display the marginalized posterior distributions for each parameter, with the 16th and 84th percentiles indicated by vertical dashed lines. The off-diagonal panels present the two-dimensional joint posterior distributions for each parameter pair, with 1σ , 2σ , and 3σ confidence contours shown as black solid lines. The red vertical solid lines indicate the best-fitting parameter values.

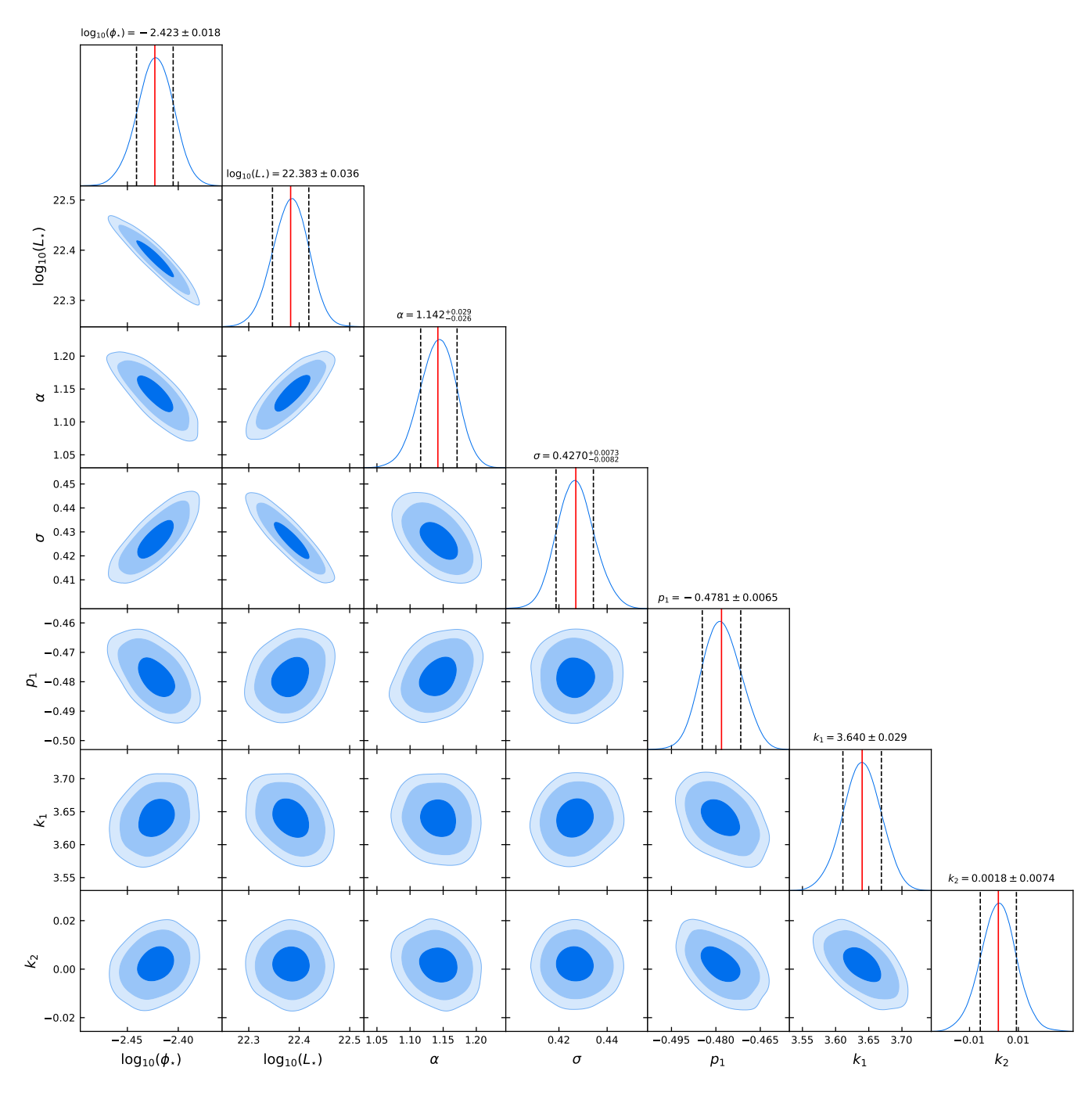


Figure 10. Similar to Figure 9, but for ELAIS-N1 field Model B.

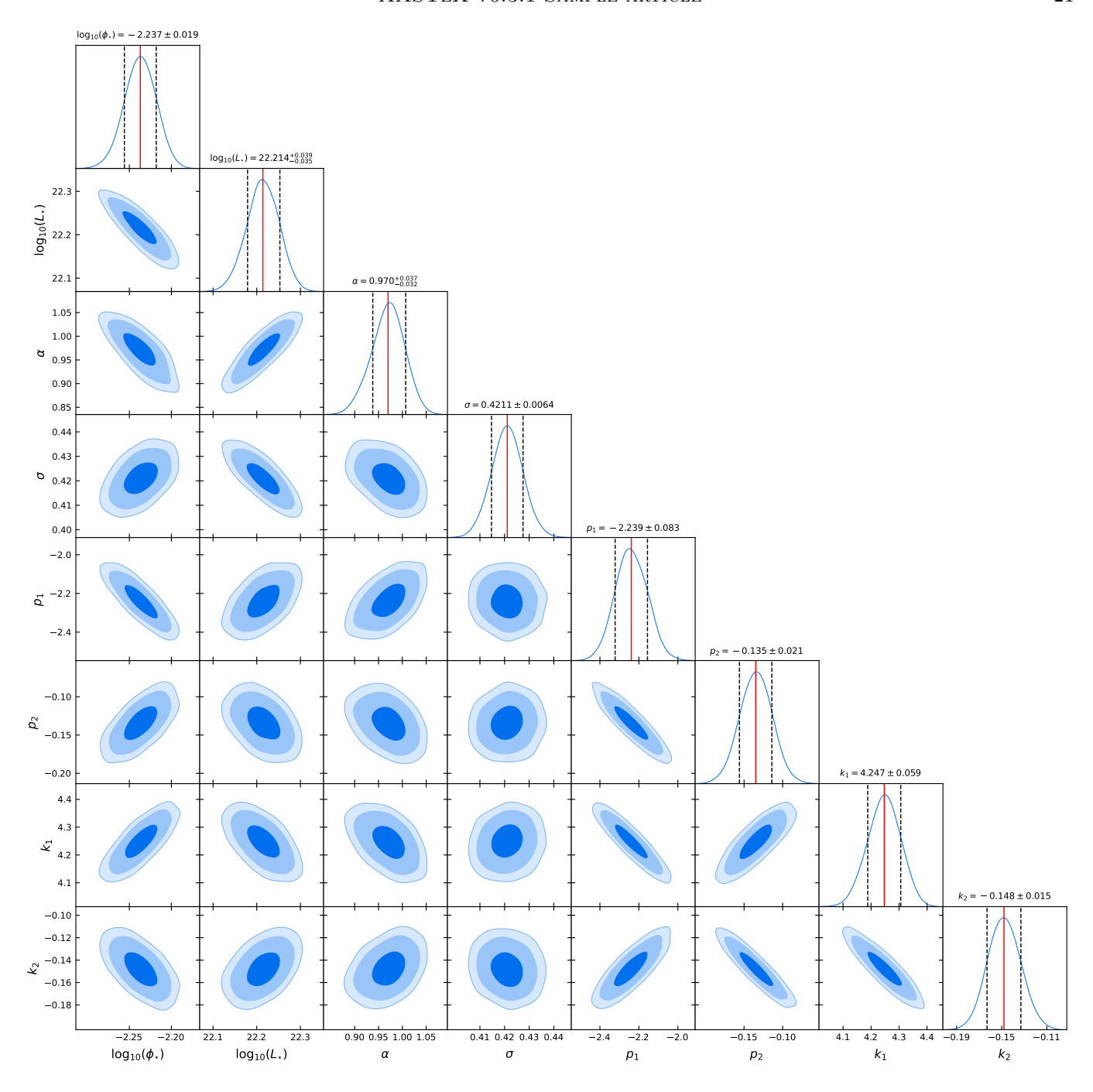


Figure 11. Similar to Figure 9, but for ELAIS-N1 field Model C.

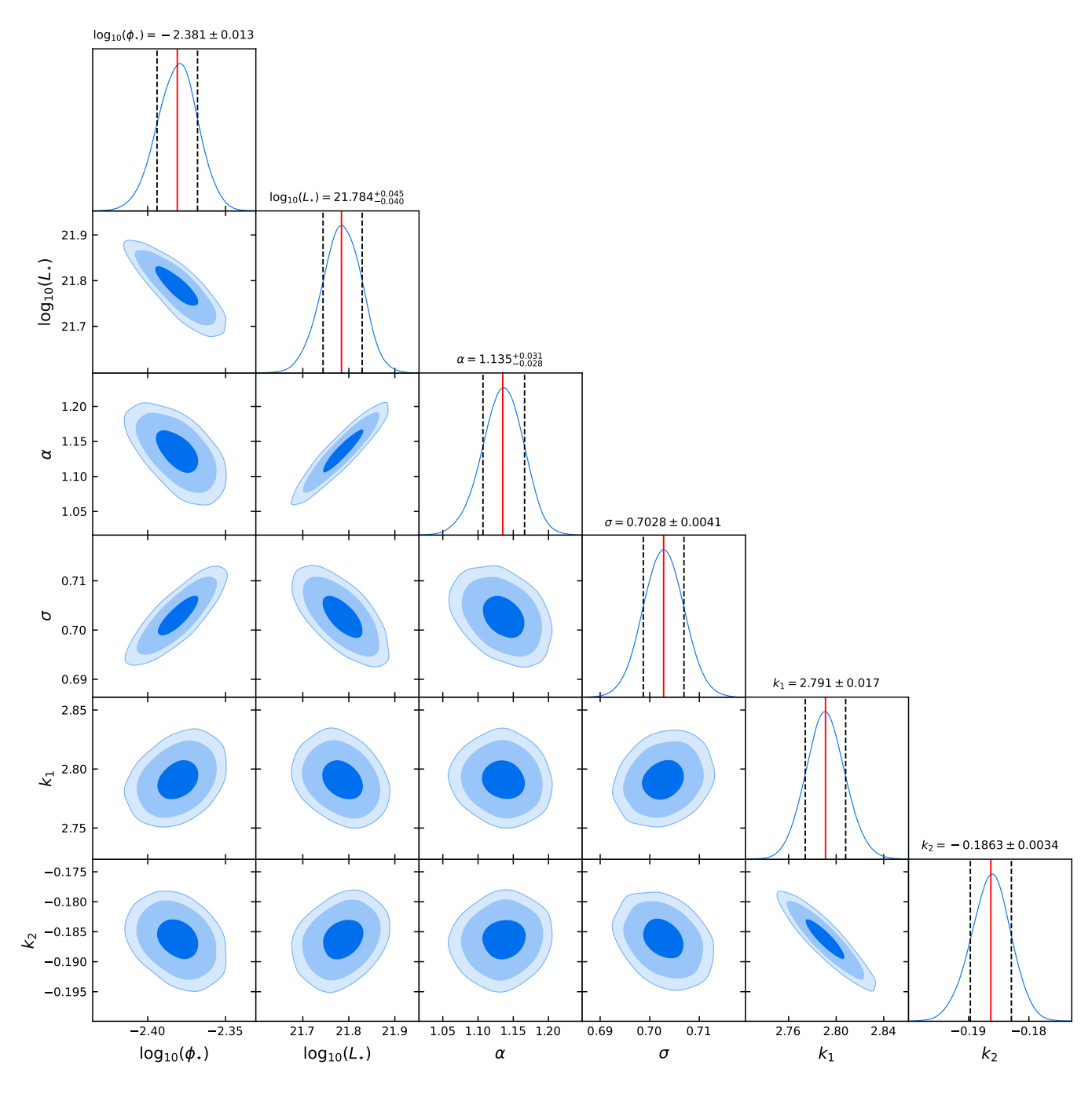


Figure 12. Similar to Figure 9, but for All fields Model A.

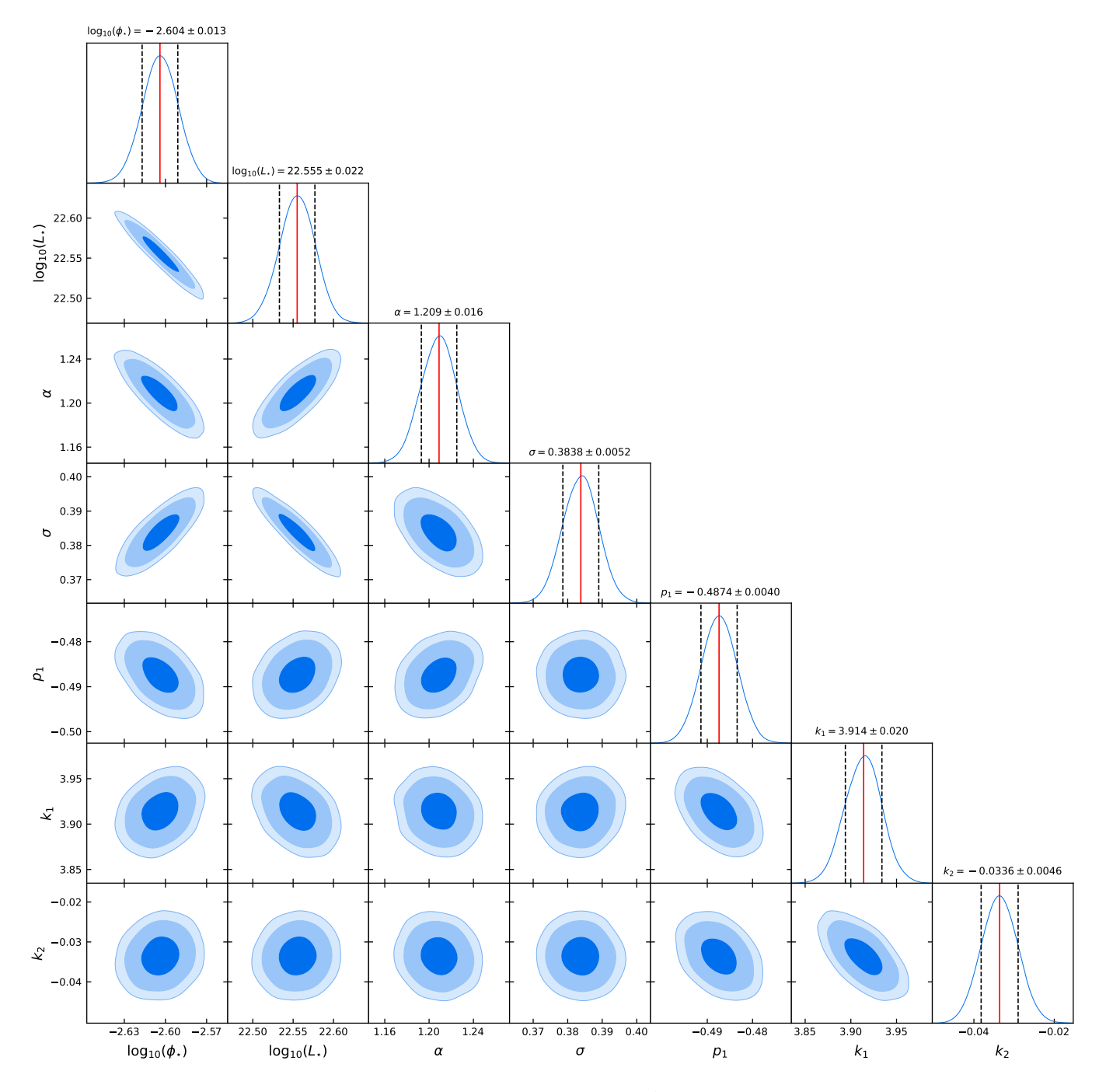


Figure 13. Similar to Figure 9, but for All fields Model B.

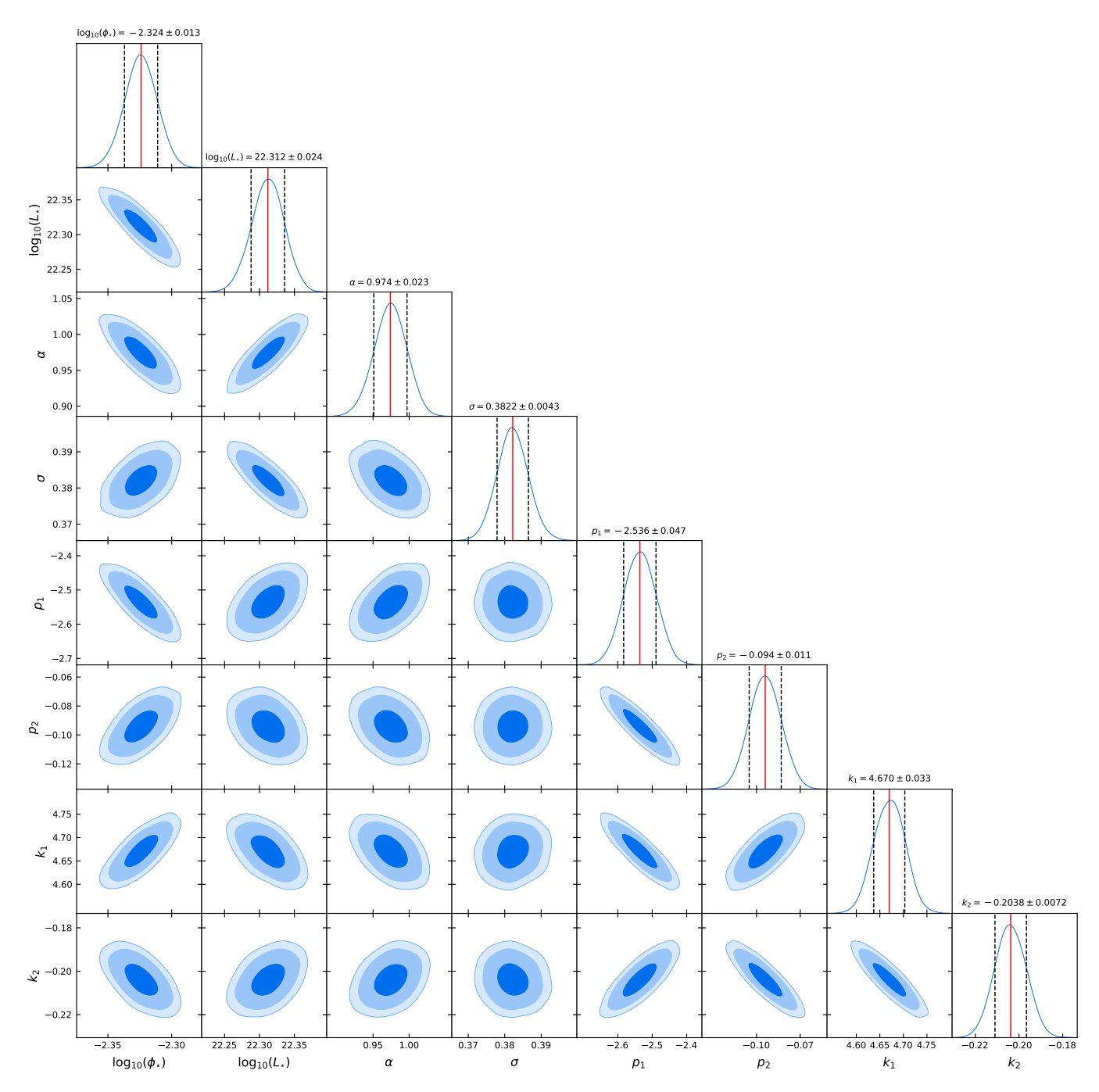


Figure 14. Similar to Figure 9, but for All fields Model C.